Monthly Notices of the ROYAL ASTRONOMICAL SOCIETY

MNRAS **542,** 790–810 (2025) https://doi.org/10.1093/mnras/staf1261
Advance Access publication 2025 July 31

Does magnetic field promote or suppress fragmentation in AGN discs? Results from local shearing box simulations with simple cooling

Tsun Hin Navin Tsung,[1,2]★ Mitchell C. Begelman,[2,3] Philip J. Armitage,[4,5] Yan-Fei Jiang(姜燕飞)[4] and Hannalore J. Gerling-Dunsmore[2,3]

[1]*Center for Integrated Plasma Studies, Physics Department, 390 UCB, University of Colorado, Boulder, CO 80309, USA*
[2]*JILA, University of Colorado and National Institute of Standards and Technology, 440 UCB, Boulder, CO 80309-0440, USA*
[3]*Department of Astrophysical and Planetary Sciences, 391 UCB, University of Colorado, Boulder, CO 80309-0391, USA*
[4]*Center for Computational Astrophysics, Flatiron Institute, 162 Fifth Avenue, New York, NY 10010, USA*
[5]*Department of Physics and Astronomy, Stony Brook University, Stony Brook, NY 11794, USA*

Accepted 2025 July 25. Received 2025 July 25; in original form 2025 June 8

ABSTRACT

Accretion discs in Active Galactic Nuclei (AGNs) are predicted to become gravitationally unstable substantially interior to the black hole's sphere of influence, at radii where the disc is simultaneously unstable to the magnetorotational instability (MRI). Using local shearing box simulations with net vertical flux and a simple cooling prescription, we investigate the effect of magnetic fields on fragmentation in the limit of ideal magnetohydrodyamics. Different levels of in-disc magnetic field from the magnetorotational instability are generated by varying the initial vertical-field plasma beta β_0. We find that the disc becomes magnetically dominated when $\beta_0 < 10^3$, and that this transition is accompanied by a drastic drop in fragmentation (as measured by the bound mass fraction) and gravitational stress. The destabilizing influence of radial magnetic fields, which are present locally and which may promote fragmentation via magnetic tension effects, is overwhelmed by magnetic elevation, which significantly reduces the mid-plane density. The magnetic suppression of fragmentation in magnetically elevated discs has implications for the radial extent of the accretion flow in AGN discs, and for the efficiency of *in situ* formation of disc-embedded stars that are progenitors for single and binary compact objects.

Key words: accretion, accretion discs – instabilities – magnetic fields – galaxies: active – quasars: supermassive black holes.

1 INTRODUCTION

Accretion discs in Active Galactic Nuclei (AGNs) are predicted to become self-gravitating via the Toomre instability (Toomre 1964) beyond a critical radius, which is a small fraction of the black hole's sphere of influence. The onset of disc self-gravity can lead to fragmentation and *in situ* star formation closer to the black hole than conventional processes allow, potentially disrupting the accretion flow and limiting black hole growth (Shlosman, Begelman & Frank 1990; Goodman 2003), but also producing compact objects and binaries that are detectable as LISA or LIGO gravitational wave sources (Levin 2007; McKernan et al. 2018).

The conditions under which gravitational instability (GI) in astrophysical discs leads to fragmentation has been studied extensively (Kratter & Lodato 2016), particularly in the context of protoplanetary discs, which can be modelled to a first approximation as non-magnetized hydrodynamic structures. In isolated discs, prompt fragmentation occurs if the cooling time is below a threshold value that is typically of the order of the local dynamical time (Gammie 2001; Rice, Lodato & Armitage 2005; Xu et al. 2025). Rapid infall can also trigger fragmentation (Kratter et al. 2010). The applicability of these hydrodynamic criteria to AGN discs, however, is rather unclear. Estimates by Menou & Quataert (2001) suggest that, except at low accretion rates, the regions of AGN discs that are self-gravitating are also well enough ionized to be in a near-ideal magnetohydrodynamic (MHD) regime. The typical magnetic field strengths at these radii are unknown. Our main focus in this work will be on the 'magnetically elevated' regime, where moderately net strong poloidal fields lead to sustained toroidal fields whose pressure is comparable to that of the disc gas or radiation (Salvesen et al. 2016; Begelman & Silk 2017). It is also possible, however, that magnetic fields could be significantly sub-thermal, as in the case of the zero-net flux magnetorotational instability (Balbus & Hawley 1998; Davis, Stone & Pessah 2010), or substantially stronger as in Magnetically Arrested Disc (MAD) models (Tchekhovskoy, Narayan & McKinney 2011). We also note recent work by Hopkins et al. (2024), Guo et al. (2025), and Squire, Quataert & Hopkins (2025) that demonstrated the formation of hyper-magnetized discs distinct from the classic α discs and magnetically-arrested discs.

Analytically, the pressure forces associated with magnetic fields are expected to act as a stabilizing influence on disc gravitational instability. However, it has long been known that in a shearing disc magnetic tension can *destabilize* gravitational instability by suppressing the stabilizing effect of Coriolis forces (Lynden-Bell 1966). In a laminar background, Elmegreen (1987) and Gammie

★ E-mail: tsunhinnavin.tsung@colorado.edu

(1996) showed analytically that this process can indeed destabilize GI modes, but that the resulting growth is transient, with a brief phase of growth usually followed by an abrupt phase of damping. It is therefore unclear, from analytic work, whether magnetic suppression of the Coriolis force survives into the non-linear regime and affects the conditions for fragmentation. A different destabilizing effect may, however, arise due to the density perturbations that are generated in the saturated state of the magnetorotational instability (MRI). Although the zero-net flux MRI saturates under near incompressible conditions, the MRI in elevated discs with net flux leads to highly inhomogeneous discs (Salvesen et al. 2016).

Early simulation work confirmed that the interplay of gravitational and magnetorotational instabilities in accretion discs is complex. Gravitational stress is reduced when magnetized turbulence develops, implying suppression of GI (Fromang et al. 2004; Fromang 2005). The MRI forms density substructures in magnetized turbulence, which can be swing-amplified to form giant clumps (Kim, Ostriker & Stone 2003). However, the magnetic field itself reduces swing-amplification (Kim & Ostriker 2001). Thus, there was the picture that while magnetic fields tend to suppress linear development of GI, the nonlinear effects of MRI turbulence may be conducive to fragmentation through generation of denser seeds. It was unclear if the magnetic-tension-enhanced gravitational instability proposed by Lynden-Bell (1966) played a role or not.

Recent local and global simulations, including resistivity to model protoplanetary discs, have identified new physical effects. MHD turbulence can be sustained in the presence of substantial Ohmic resistivity, via a kind of spiral-wave (gravitational) dynamo that is distinct from the MRI (Riols & Latter 2019; Riols et al. 2021; Löhnert & Peeters 2023). Moreover, in high resolution global simulations, fragmented clumps form that are smaller in size than in the hydrodynamic case (Deng, Mayer & Helled 2021; Kubli, Mayer & Deng 2023). The clumps are also more numerous and long-lasting. These results have been interpreted as being due to the destabilizing effect of magnetic fields in low shear regions of the disc. As the clumps form, the magnetic field surrounding them would also be enhanced, shielding them from break-up by the shear flow, making them long-lasting. This paints a picture in which magnetic turbulence promotes fragmentation both linearly and non-linearly.

Here, we revisit the question of whether magnetic fields stabilize or destabilize AGN discs to gravitational instability, using local shearing box simulations in ideal MHD. We vary the strength of the net vertical field to induce differing levels of saturated magnetic pressure and disc elevation. The thermodynamics is modelled with a simple 'β cooling' law, both for comparison with prior work (Gammie 2001) and to efficiently explore parameter space in preparation for forthcoming radiation hydrodynamic simulations. We investigate whether the magnetic tension enhanced gravitational instability, which we refer to as the 'Coriolis-Restricted-Magneto-Gravitational' (CRMG) instability, contributes to fragmentation. Our approach is to evaluate the physical conditions (e.g. magnetic field structure, density, etc.) of the disc when the MRI is fully developed and to identify clumps through a numerical procedure. We then explain the fragmentation behavior by examining the WKB linear growth rate. Despite changing conditions in a turbulent disc, we argue that the WKB approach provides insight into the stability of the disc in an averaged sense.

The structure of this paper is as follows: In Section 2, we describe our model and simulation setups, and describe the diagnostics we use in Section 3. In Section 4, we briefly outline the theory of how magnetic fields can destabilize GI. We describe our simulation results in Section 5 and conclude in Section 6.

2 SIMULATION SET-UP

We utilize the 3D shearing-box set-up in `Athena++` (Stone et al. 2020) to solve the ideal magnetohydrodynamic (MHD) equations:

$$\frac{\partial \rho}{\partial t} + \nabla \cdot (\rho \mathbf{v}) = 0, \tag{1}$$

$$\frac{\partial (\rho \mathbf{v})}{\partial t} + \nabla \cdot \left(\rho \mathbf{v}\mathbf{v} - \mathbf{B}\mathbf{B} + P_g + B^2/2\right) = -2\rho\Omega\hat{\mathbf{z}} \times \mathbf{v} \tag{2}$$

$$+2q\rho\Omega^2 x\hat{\mathbf{x}} - \rho\Omega^2 z\hat{\mathbf{z}} - \rho\nabla\Phi,$$

$$\frac{\partial E}{\partial t} + \nabla \cdot \left[\left(E + P_g + B^2/2\right)\mathbf{v} - \mathbf{B}(\mathbf{B}\cdot\mathbf{v})\right] = -\rho\mathbf{v}\cdot\nabla\Phi \tag{3}$$

$$\rho\Omega^2\mathbf{v}\cdot(2qx\mathbf{x} - z\hat{\mathbf{z}}) - \frac{E_{\rm th}}{\tau_{\rm cool}},$$

$$\frac{\partial \mathbf{B}}{\partial t} = \nabla \times (\mathbf{v} \times \mathbf{B}), \tag{4}$$

where $E = \rho v^2/2 + P_g/(\gamma - 1) + B^2/2$ is the total (kinetic + thermal + magnetic) energy density, $E_{\rm th} = P_g/(\gamma - 1)$ is the thermal energy density, Ω is the angular velocity at the origin, about which the shearing-box approximation is made, q is the shearing parameter (3/2 for Keplerian potential), and $\tau_{\rm cool}$ is the cooling time. We take $\gamma = 5/3$ to be the adiabatic index of the gas. The x, y, z-axes represent the radial, azimuthal and vertical directions, respectively. The gravitational potential Φ is calculated from Poisson's equation,

$$\nabla^2\Phi = 4\pi G\rho. \tag{5}$$

The MHD equations are solved using a Godunov method, a second-order van Leer time integrator, the HLLD Riemann solver to calculate the hydrodynamic fluxes together with the constrained transport (CT) technique to ensure the magnetic field is divergence-less (Stone et al. 2020). Poisson's equation is solved using Fast Fourier Transform (FFT) (Koyama & Ostriker 2009; Kim, Kim & Ostriker 2011).

The initial profile is characterized by

$$Q = \frac{\Omega^2}{2\pi G\rho_0}, \tag{6}$$

which we call the proxy Toomre parameter due to its relationship to the actual Toomre parameter Q_T initially (see Appendix A). Assuming a uniform, vertical magnetic field, no x, z flow and that ρ, P_g depend only on z, the initial profile can be evaluated by setting the time derivative of equation (2) to zero. This gives a steady-state solution $\mathbf{v} = -q\Omega x\hat{\mathbf{y}}$ for the velocity, and the following equation for ρ, P_g:

$$\frac{1}{\rho}\frac{{\rm d}P_g}{{\rm d}z} = -\Omega^2 z - 4\pi G\int_0^z \rho\,{\rm d}z', \tag{7}$$

which can be solved numerically assuming a polytropic EOS, provided the mid-plane density ρ_0 and gas pressure P_{g0} are known. In practice, the surface density Σ and angular velocity Ω are more easily obtained. (ρ_0, P_{g0}) can be determined from (Σ, Ω) using the fact that

$$\Sigma = 2\int_0^\infty \rho\,{\rm d}z\,, \quad \Omega^2 = 2\pi G\rho_0 Q. \tag{8}$$

The details of the calculation are described in Appendix A. It can be shown, given Q, Σ, Ω, that the mid-plane density, gas pressure and temperature are given by

$$\rho_0 = \frac{\Omega^2}{2\pi G Q}, \quad P_{g0} = \frac{2\Sigma\Omega^2}{5Q\Psi_{3/2}}, \quad T_0 = \left(\frac{\mu m_p}{k_{\rm B}}\right)\frac{4\pi G\Sigma}{5\Psi_{3/2}}, \tag{9}$$

where $\Psi_{3/2}(Q)$ is a dimensionless measure of a disc's thickness dependent only on Q. For $Q \ll 1$, where self-gravity dominates, $\Psi_{3/2}$ will be small, while $\Psi_{3/2}$ asymptotes to a constant value for $Q \gg 1$, when the tidal potential dominates. For constant Q, $\rho_0 \propto \Omega^2$, $P_{g0} \propto \Sigma\Omega^2$, $T_0 \propto \Sigma$, while for constant Σ and Ω, ρ_0, P_{g0}, T_0 decrease for increasing Q.

The simulations were performed in code units. We define the time unit to be $t_* = \Omega^{-1}$, length unit to be the scale-height evaluated at the mid-plane $l_* = H = c_{s0}/\Omega$, density unit to be the mid-plane density $\rho_* = \rho_0$, velocity unit to be the mid-plane sound speed $v_* = c_{s0}$, pressure unit $P_* = \rho_* v_*^2$, temperature unit $T_* = \mu m_p P_*/k_B\rho_*$ ($\mu = 0.6$ is the mean molecular weight per m_p), and magnetic field unit $B_* = \sqrt{4\pi P_*}$. With this unit system, the unit gravitational potential is defined as $\Phi_* = v_*^2$ and '$4\pi G$' in code units by $4\pi G\rho_* t_*^2 = 2/Q$. The initial density and pressure profiles in code units are completely specified given Q.

We use a fiducial box domain of $20H \times 20H \times 24H$ for our investigation. A long vertical span is necessary to ensure that a sufficient number of non-linear density scale heights are captured and to reduce boundary effects associated with a magnetically elevated disc. A wide horizontal span is needed for gravitational effects, which are long-range, to operate. For the strongly magnetized cases ($\beta_0 \leq 10^2$, where β_0 is the initial mid-plane plasma beta), we set the azimuthal box length to be 2 times the radial (i.e. $20H \times 40H \times 24H$) to suppress strong zonal flows that form in the highly magnetized cases, a magnetic-wind-driven feature (Riols & Lesur 2019) that can artificially increase fragmentation rates (see Appendix B for more details). We adopt shearing-periodic boundary conditions in the x-direction and periodic boundaries in the y-direction. For the boundaries in the z-direction, we enforce outflow conditions for ρ, P_g, v_x, v_y and impose outflow conditions for v_z when the gas is outflowing and set the ghost zones $v_z = 0$ when it is inflowing. For magnetic fields we follow Riols & Latter (2019) and Löhnert & Peeters (2023) to set $B_x = B_y = 0$ in the ghost zones and $\mathrm{d}B_z/\mathrm{d}z = 0$. We find that such magnetic boundary conditions generally lead to a shorter simulation runtime than outflow boundaries (Bai & Stone 2013) due to the reduced Alfvén speed close to the boundaries. We note that while this is an often adopted recourse in shearing box simulation, setting $B_x = B_y = 0$ at the vertical boundaries prevents a magnetic exchange of angular momentum between the outflow/wind and the disc, particularly if there is a magnetized wind.

We impose an initial magnetic field with a net vertical flux in the form (Salvesen et al. 2016)

$$B_z = B_0\left[1 + \frac{1}{2}\sin\left(\frac{2\pi x}{L_x}\right)\right], \tag{10}$$

where L_x is the domain width in the x-direction. The sinusoidal component in equation (10) is there to suppress channel flows, which could lead to rapid depletion of the disc mass. B_0 is specified through the mid-plane plasma beta $\beta_0 = 2P_{g0}/B_0^2$. Simulations with net vertical flux are always found to launch strong outflows that can drain the box mass in tens of orbits. To produce a steady-state solution, we therefore add mass in the form $\propto \exp(-z^2/H^2)$ (where H is the initial scale height defined by the mid-plane c_{s0}) to each grid cell at the end of each iteration to keep the total mass within the box constant, mimicking mass supply from accretion.

We implement cooling through an explicit source term using a simplistic cooling model $t_{\rm cool} = \tau_{\rm cool}\Omega^{-1}$ (Gammie 2001) such that

$$\frac{\mathrm{d}E_{\rm th}}{\mathrm{d}t} = -\frac{E_{\rm th}\Omega}{\tau_{\rm cool}}. \tag{11}$$

This simple prescription, though not realistic, has the advantage of being freely adjustable and has been used widely in the literature (Gammie 2001; Rice et al. 2005; Meru & Bate 2010).

We trigger MRI by generating white noise on the initial density and velocities having maximum amplitude of $|\delta\rho|/\rho = 0.01$ and $|\delta v_i/c_s| = 0.01$, respectively.

We vary the initial mid-plane plasma beta β_0 through $10, 10^2, 10^3, 10^4, 10^5$ to investigate the effect of magnetic field on fragmentation and set the cooling time $\tau_{\rm cool} = 1$. We choose $\tau_{\rm cool}$ to be less than 3, the fragmentation condition in the non-magnetized case (Gammie 2001), to ensure fragmentation in the weakly magnetized cases. We cannot set $\tau_{\rm cool}$ below 1 as the cooling time could easily be less than the signal travel time across a grid (i.e. $\Delta x/\max(v_A, c_s, v)$) for the weakly magnetized cases during run-time, leading to artificial heating and code crashing. We set $Q = 1$ initially for all our simulations. This sets the initial setup to be marginally Toomre unstable, with a Toomre parameter $Q_T = 0.89$ (equation A6). The exact choice of Q is not important provided the initial magnetic field is sub-thermal and cooling is fast compared to timescales of the MRI, as the disc will be cooled below $Q_T = 1$ on the cooling time-scale even if $Q_T > 1$ initially.

The simulation box is resolved with a fiducial resolution of $256 \times 256 \times 512$ for the $\beta_0 \geq 10^3$ cases and $256 \times 512 \times 384$ for the $\beta_0 \leq 10^2$ cases. We use a coarser vertical grid size for the low β_0 cases as the MRI scale is larger, but double the number of grids in the azimuthal direction due to the larger azimuthal domain width. As shown in Table 1, the quality factors in the y, z directions Q_y, Q_z are quite large in the saturated regime, meaning that MRI scales are likely resolved. We repeat our simulations at a reduced resolution of resolution of $128 \times 256 \times 192$ (for $\beta_0 \leq 10^2$) and $128 \times 128 \times 192$ (for $\beta_0 \geq 10^3$) and compare our results in Appendix G. To avoid excessive simulation cost associated with small time-steps in magnetically dominated regions, we impose a density floor of $\rho_{\rm floor} = 10^{-4}\rho_0$. We also impose a temperature floor of $T_{\rm floor} = 10^{-5}T_0$ and ceiling of $T_{\rm ceil} = 10^2 T_0$ to avoid numerical difficulties associated with excessive cooling and large sound speeds.

3 DIAGNOSTICS

We adopt the following notations to denote various averages used in our analysis and discussion. First, we define $\langle X\rangle_{xy}$ as horizontally averaged quantities:

$$\langle X\rangle_{xy} = \frac{1}{L_x L_y}\int X\,\mathrm{d}x\,\mathrm{d}y\,, \tag{12}$$

where L_x, L_y are the domain widths in the x, y-directions, respectively. Next, we define $\langle X\rangle_V$ as volume averaged quantities:

$$\langle X\rangle_V = \frac{1}{L_x L_y L_z}\int X\,\mathrm{d}x\,\mathrm{d}y\,\mathrm{d}z\,, \tag{13}$$

where L_z is the domain height in the z-direction. We will occasionally consider mass averaged quantities as well, defined by:

$$\langle X\rangle_\rho = \frac{\int \rho X\,\mathrm{d}x\,\mathrm{d}y\,\mathrm{d}z}{\int \rho\,\mathrm{d}x\,\mathrm{d}y\,\mathrm{d}z}. \tag{14}$$

We also define $\langle X\rangle_t$ as time averaged quantities:

$$\langle X\rangle_t = \frac{1}{t_f - t_i}\int_{t_i}^{t_f} X\,\mathrm{d}t'\,, \tag{15}$$

where t_i, t_f are the initial and final times the average is taken through, to be defined upon usage. To assess the effect of gravitation, it is

Table 1. Simulation parameters and transport quantities of the different simulations. $\langle\cdot\rangle_t$ denotes time-averaged quantities taken over $\Omega t = 100 - 300$, except for the $\beta_0 = 10^5$ case, which is taken over $\Omega t = 250 - 450$. Q_y, Q_z are the quality factors in the y, z-direction, $Q_y = 2\pi v_{A,y}/\Omega\Delta y$, $Q_z = 2\pi v_{A,z}/\Omega\Delta z$.

β_0	domain	grid	$\langle Q_y\rangle_t$	$\langle Q_z\rangle_t$	$\langle\langle\alpha_M\rangle_V\rangle_t$	$\langle\langle\alpha_R\rangle_V\rangle_t$	$\langle\langle\alpha_G\rangle_V\rangle_t$
10	$20H \times 40H \times 24H$	$256 \times 512 \times 384$	482	146	3.28	0.788	0.00125
10^2	$20H \times 40H \times 24H$	$256 \times 512 \times 384$	391	88.2	1.34	0.305	0.00111
10^3	$20H \times 20H \times 24H$	$256 \times 256 \times 512$	207	35.8	1.15	0.224	0.0124
10^4	$20H \times 20H \times 24H$	$256 \times 256 \times 512$	78.6	24.8	0.461	0.302	0.132
10^5	$20H \times 20H \times 24H$	$256 \times 256 \times 512$	82.5	28.7	0.380	0.320	0.132

useful to define the Toomre parameter Q_T and the magnetic Toomre parameter $Q_{T,B}$ (Kim & Ostriker 2001) as

$$Q_T = \frac{\langle c_s^2\rangle_\rho^{1/2}\kappa}{\pi G\Sigma}, \quad Q_{T,B} = \frac{\langle c_s^2 + v_A^2\rangle_\rho^{1/2}\kappa}{\pi G\Sigma}, \tag{16}$$

where $v_A^2 = B^2/\rho$ is the Alfvén speed, $\kappa = \sqrt{2(2-q)}\Omega$ is the epicyclic frequency (note that for Keplerian shear $\kappa = \Omega$). Q_T of the initial profile is related to Q through equation (A6). For $Q = 1$, which is used throughout the study in the initial set-up, $Q_T = 0.89$. In this study, we often have to examine the stresses, as they are important to angular momentum and energy transport in accretion flows. The Reynolds, Maxwell and gravitational stress are defined respectively by

$$T^R_{r\phi} = \rho v_x \delta v_y, \quad T^M_{r\phi} = -B_x B_y, \quad T^G_{r\phi} = \frac{g_x g_y}{4\pi G}, \tag{17}$$

where $\delta v_y = v_y + q\Omega x$ denotes the deviation of v_y from the equilibrium flow. The α stresses, which are dimensionless measures of the stress, are defined by dividing the stresses by the gas pressure. The horizontally averaged mid-plane and volume averaged Reynolds, Maxwell and gravitational α parameters are defined by

$$\langle\alpha_R\rangle_V = \frac{\langle T^R_{r\phi}\rangle_V}{\langle P_g\rangle_V}, \ \langle\alpha_M\rangle_V = \frac{\langle T^M_{r\phi}\rangle_V}{\langle P_g\rangle_V}, \ \langle\alpha_G\rangle_V = \frac{\langle T^G_{r\phi}\rangle_V}{\langle P_g\rangle_V}. \tag{18}$$

Finally, we define $\bar{X}_w$ as the 'window' average in the x, y-direction:

$$\bar{X}_w = \frac{1}{w^2}\int_{x-w/2}^{x+w/2}\int_{y-w/2}^{y+w/2} X\,\mathrm{d}x'\,\mathrm{d}y', \tag{19}$$

where w is some specified 'window' width over which this average is taken. Assuming a variable X is expressed as a sum of Fourier modes

$$X = \int_{-\infty}^{\infty}\tilde{X}_{k_x,k_y}\cos(k_x x + \phi)\cos\left(k_y y + \phi'\right)\mathrm{d}k_x\,\mathrm{d}k_y, \tag{20}$$

then its window-average

$$\begin{aligned}\bar{X}_w = \frac{1}{w^2}&\int_{x-w/2}^{x+w/2}\int_{y-w/2}^{y+w/2}\int_{-\infty}^{\infty}\tilde{X}_{k_x,k_y}\cos\left(k_x x' + \phi\right)\\ &\times\cos\left(k_y y' + \phi'\right)\mathrm{d}k_x\,\mathrm{d}k_y\,\mathrm{d}x'\,\mathrm{d}y'\end{aligned} \tag{21}$$

$$\begin{aligned}= &\int_{-\infty}^{\infty}\int_{-\infty}^{\infty}\tilde{X}_{k_x,k_y}\cos(k_x x + \phi)\cos\left(k_y y + \phi'\right)\\ &\times\frac{\sin(k_x w/2)}{(k_x w/2)}\frac{\sin\left(k_y w/2\right)}{(k_y w/2)}\mathrm{d}k_x\,\mathrm{d}k_y,\end{aligned} \tag{22}$$

so contributions of modes with wavenumber $k_x w, k_y w > 1$ is suppressed. This represents a smoothing procedure, or convolution, in the x, y-direction. When operating on real data, the upper and lower limits of the integral in equation (19) are replaced by $x_{\max}$, $x_{\min}$ and $y_{\max}$, $y_{\min}$ when the domain limits are exceeded.

3.1 Clump identification

To assess disc fragmentation quantitatively, we follow the procedure outlined in Chen et al. (2023), using a 3D extension of the GRID-core algorithm (Gong & Ostriker 2011; Mao, Ostriker & Kim 2020). Briefly, for each local minimum in the gravitational potential field Φ, we first identify the closed contour with the largest value of $\Phi = \Phi_{\max}$, which contains no other local minima. This region, which is referred to as a *gravitational binding region* (GBR), satisfies

$$\int_{\mathrm{GBR}}\rho(\Phi - \Phi_{\max})\,\mathrm{d}V < 0. \tag{23}$$

Within a GBR, we narrow the region down to cells where

$$\int_{\mathrm{TBR}} E_{\mathrm{kin}} + E_{\mathrm{th}} + E_B + \rho(\Phi - \Phi_{\max})\,\mathrm{d}V < 0 \tag{24}$$

is satisfied when integrated up to some sub-contour $\Phi' < \Phi_{\max}$, for which the gas is gravitationally bound against turbulent, thermal and magnetic pressure. Such a region is called a *Total Binding Region* (TBR). Here, E_{kin} is the kinetic energy density relative to the center of mass ($E_{\mathrm{kin}} = 0.5\rho\delta\mathbf{v}^2_{\mathrm{CM}}$, where $\delta\mathbf{v}_{\mathrm{CM}} = \mathbf{v} - \mathbf{v}_{\mathrm{CM}}$ and $\mathbf{v}_{\mathrm{CM}}$ is the centre of mass velocity of the clump), E_{th} is the thermal energy density, and E_B is the magnetic energy density. The whole GBR can be a TBR if the gravitational well is deep enough. In Fig. 1, we show an example of clump identification using this algorithm, where the black-solid and red-dashed contours denote GBR and TBR, respectively, overlaid on the mid-plane density and gravitational potential snapshot at $\Omega t = 200$.

4 THEORETICAL CONSIDERATIONS

Magnetic field is often viewed as a stabilizing agent against gravitational collapse due to magnetic pressure support, counteracting gravity in linear stability analysis of the Jeans instability. On the other hand, in a rotating and shearing disc, magnetic tension can reduce the stabilizing influence of Coriolis force, leading to *enhanced* gravitational instability (Lynden-Bell 1966; Elmegreen 1987; Gammie 1996; Kim & Ostriker 2001). These competing effects of magnetic field raise the question of whether one effect would dominate the other in a realistic scenario, i.e. whether magnetic field *promotes* or *suppresses* gravitational instability or fragmentation. We find that this question has not been fully addressed in an MRI-turbulent disc. Past studies have focused on the mutual effects of gravitoturbulence and MRI in a mildly cooling disc (Löhnert & Peeters 2023) and gravitoturbulence as a dynamo mechanism (especially in the context of a protoplanetary disc, where the gas may not be fully ionized and MRI may not be active, e.g. Riols & Latter 2019; Deng, Mayer & Latter 2020; Riols et al. 2021; Béthune & Latter 2022). We find it important to address the fragmentation aspect of this problem in order to better understand accretion flows and production of gravitational wave sources in AGN discs. In this section, we outline how magnetic tension could enhance gravitational instability in a

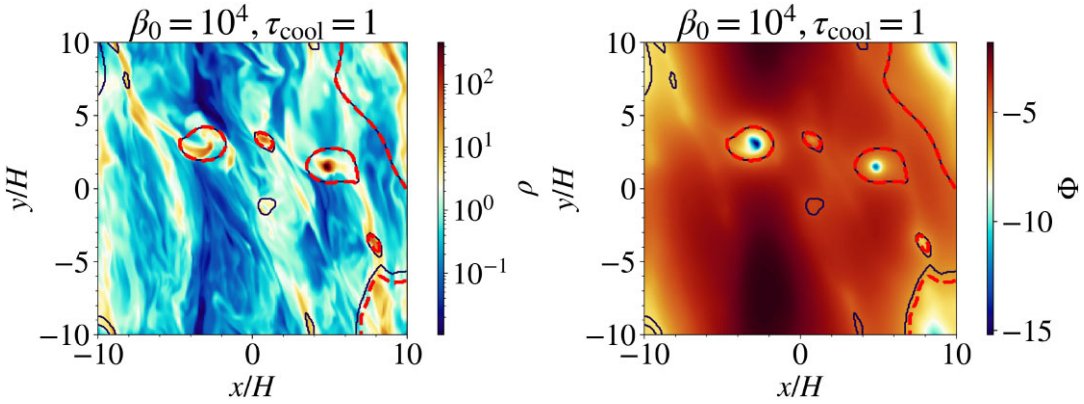

Figure 1. Clump identification using the extended GRID algorithm, with black-solid and red-dashed contours denoting GBR and TBR, respectively, overlaid on a mid-plane density (left) and gravitational potential (right) snapshot at $\Omega t = 200$ for the $\beta_0 = 10^4$, $\tau_{\rm cool} = 1$ case.

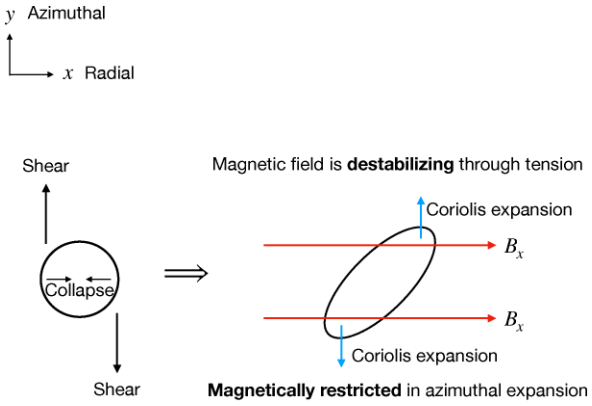

Figure 2. Intuition for the Coriolis-Restricted-Magneto-Gravitational (CRMG) instability. An overdense blob undergoing gravitational collapse experiences Coriolis forces which tend to expand it. This expansion is restricted by magnetic tension if a strong radial field is present, which promotes further collapse.

rotating, shearing disc, lay out possible reasons why this effect has received little attention in the past, and offer new insights into why we reconsidered it in this study. The discussion in this section will motivate our specific focus in the results section (Section 5).

4.1 Magnetic destabilization of gravitational modes

An overdense blob generated from random motion and undergoing gravitational collapse experiences Coriolis forces which tend to expand it. This expansion is restricted by magnetic tension if a strong radial field is present, which promotes further collapse (Fig. 2). We call this mechanism by which magnetic fields destabilize GI the Coriolis-Restricted-Magneto-Gravitational (CRMG) instability.

Following the local WKB stability analysis carried out in Appendix C, axisymmetric perturbations in a rotating, razor-thin disc subjected to an in-disc magnetic field $\mathbf{B} = B_x\hat{\mathbf{x}} + B_y\hat{\mathbf{y}}$ exhibit characteristic modes with the dispersion relation (Gammie 1996)

$$\omega^4 + \left[2(q-2)\Omega^2 - k_x^2\left(c_s^2 + v_A^2\right) + 2\pi G\Sigma_0|k_x|\right]\omega^2 + iq\Omega\omega k_x^2 v_{Ax} v_{Ay} + k_x^2 v_{Ax}^2\left(c_s^2 - 2\pi G\Sigma_0|k_x|\right) = 0, \quad (25)$$

where $\mathbf{v}_A = \mathbf{B}/\sqrt{\Sigma_0}$ is the Alfvén velocity, $c_s = \sqrt{\gamma P_g/\Sigma_0}$ is the sound speed, k_x is the axisymmetric wavenumber, q is the shearing rate, and Σ_0 is the surface density. In this discussion, we focus on axisymmetric modes due to the simplicity of the analysis. Stability analysis can be performed on non-axisymmetric modes as well (see Appendix C), but they generally do not admit WKB solutions due to fast variations of the non-axisymmetric wavevector. While this analysis assumes a razor-thin disc, in practice discs always have finite thickness, and in magnetically elevated disc scenarios it may be more appropriate to assume the background is approximately uniform instead of razor-thin at the mid-plane. In this case, the dispersion relation equation (25) is modified by replacing the $2\pi G\Sigma_0|k_x|$ terms by $4\pi G\rho_0$ (equation C21). First consider the limit in which there is no rotation ($\Omega = 0$): the dispersion relation equation (25) reduces to

$$\omega^2 = k_x^2 v_{Ax}^2, \quad \omega^2 = k_x^2\left(c_s^2 + v_{Ay}^2\right) - 2\pi G|k_x|\Sigma_0, \quad (26)$$

the former which are simply Alfvén waves and the latter magneto-Jeans type modes[1]. Magnetic field is a stabilizing agent or simply a medium of oscillatory wave propagation in this case. In the other limit, in which there is no radial field ($v_{Ax} = 0$), equation (25) reduces to

$$\omega^2 = k_x^2\left(c_s^2 + v_{Ay}^2\right) + 2(2-q)\Omega^2 - 2\pi G|k_x|\Sigma_0, \quad (27)$$

which again is a magneto-Jeans type mode with rotation as an additional stabilizing influence, again stabilized by magnetic field. These two limits are uninteresting for the current discussion, due to the stabilizing effect of magnetic fields. It is more interesting to consider parameters away from these limits, for which magnetic fields are destabilizing. Specifically, if there is rotation and the magnetic field has a radial component ($B_x/B \neq 0$), one can solve equation (25) numerically and identify the most unstable root. The growth rate depends on 5 dimensionless parameters: the axisymmetric wavenumber $k_x V_A/\Omega$, the Toomre parameter $Q_T = c_s\kappa/\pi G\Sigma_0$, the in-disc plasma beta $\beta_{\rm disk} = 2P_g/(B_x^2 + B_y^2)$, orientation of the in-disc magnetic field $b_x = B_x/(B_x^2 + B_y^2)^{1/2}$, and the shearing rate q.

In Fig. 3, we show examples of the growth rates γ/Ω of such modes as a function of the axisymmetric wavenumber $k_x v_A/\Omega$ for various in-disc plasma betas $\beta_{\rm disk}$ (top left), Toomre parameters Q_T

[1]Here, we define magneto-Jeans modes as wave modes that follow the dispersion relation $\omega^2 = k_x^2(c_s^2 + v_A^2) + 2(2-q)^2\Omega^2 - 2\pi G|k_x|\Sigma_0$ or close variations of this, in which magnetic field is a stabilizing influence. This definition is different from that used in Kim & Ostriker (2001). If the background is uniform instead of razor-thin, the dispersion relation becomes $\omega^2 = k_x^2(c_s^2 + v_A^2) + 2(2-q)^2\Omega^2 - 4\pi G\rho_0$ instead, i.e. replacing the $2\pi G|k_x|\Sigma_0$ term by $4\pi G\rho_0$.

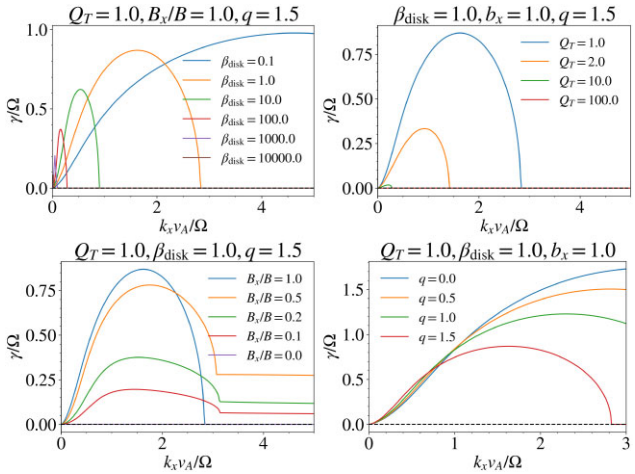

Figure 3. Growth rates γ (normalized by Ω) of axisymmetric perturbations ($k_y = 0$) as a function of $k_x v_A/\Omega$ for various $\beta_{\rm disk} = 2P_g/(B_x^2 + B_y^2)$ (top left), Toomre parameters $Q_T = c_s\Omega/\pi G\Sigma_0$ (top right), orientations of the magnetic field $b_x = B_x/(B_x^2 + B_y^2)^{1/2}$ (lower left), and shearing rates q (lower right) while the other variables are kept fixed at values listed at the top of each panel.

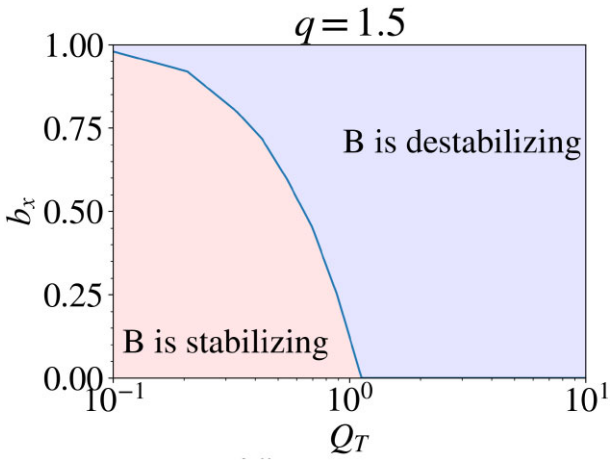

Figure 4. Plot of $b_{x,\rm thres}$ against Q, demarcating region where the magnetic field is destabilizing (above the curve, shaded in blue) and vice versa.

(top right), magnetic field orientations b_x (lower left), and shearing rates q (lower right) while fixing the other parameters. We observe clearly in the top left panel that CRMG modes are more unstable in stronger magnetic fields for the same Q_T, both in terms of the maximum growth rate and the range of wavenumbers that are unstable. When maximally unstable, this instability acts fast, on the timescale of $\sim \Omega^{-1}$. The top right panel shows that CRMG modes are more unstable at lower Q_T, cementing it as a gravitational mode. However, unlike Toomre modes, which require $Q_T < 1$ (or even smaller for strong magnetic fields) to be unstable, the CRMG instability criteria are more lenient on Q_T, as modes can be unstable even for $Q_T > 1$, albeit with smaller growth rates and more restrictive ranges of unstable wavenumbers. The orientation of the magnetic field also impacts the growth rate – as shown in the lower left panel, the instability appears weaker as the magnetic field veers off from the radial direction into the azimuthal, with the instability subdued when the field is completely azimuthal, at right angles to the axisymmetic wavevector[2]. This point is quite important, and we will refer to it again in the following discussion. Finally, the lower right panels shows that CRMG modes are more unstable for lower shearing rates due to reduced Coriolis stabilization.

In short, axisymmetric perturbations in a self-gravitating flow subjected to shear and an in-disc magnetic field become *more* unstable with respect to a stronger field when there is a radial component in the background field, for constant Toomre parameter Q_T. When the field is completely azimuthal, the effect of magnetic field is *stabilizing* and one recovers the magneto-Jeans type mode. We relegate more detailed discussion of the wavelength dependence of the CRMG modes, comparision between the CRMG and the magneto-Jeans type mode, and numerical verification of the growth rates to Appendix D–F.

[2]Technically, axisymmetric modes can be unstable even when the field is completely azimuthal. One simply recovers a Magneto-Jeans type mode (equation 27), in which the instability condition is $Q_{T,B} < 1$ (Kim & Ostriker 2001). This is why in the lower left panel of Fig. 3, where $Q_T = 1 < Q_{T,B}$, the system is stable when $B_x/B_0 = 0$. Magnetic field acts as a stabilizing agent in this case.

We pointed out that magnetic field destabilizes axisymmetric CRMG modes when the field is radial, becoming stabilizing when the field is toroidal. Mathematically, this means that when $b_x = B_x/(B_x^2 + B_y^2)^{1/2}$, the relative contribution of the radial component to the in-disc field, is close to unity, the growth rate increases when $\beta_{\rm disc}$ decreases. In contrast, if the field is largely toroidal, $b_x \approx 0$, the growth rate decreases when $\beta_{\rm disk}$ decreases. The transition from destabilization to stabilization occurs at some intermediate value of b_x, which we call $b_{x,\rm thres}$. In Fig. 4, we plot $b_{x,\rm thres}$ as a function of Q_T for $q = 1.5$. The area under the curve denotes values of b_x for which the magnetic field is stabilizing, and vice versa for the area above the curve. Studies have found that Q_T maintains a value slightly above 1 in the non-linear saturation stage when GI/fragmentation occurs (Gammie 2001). On the other hand, b_x can take on an appreciable value in MRI simulations with strong vertical fluxes. These observations suggest magnetic destabilization of gravitational modes is entirely possible.

Despite the promising signs shown by this WKB analysis that strong magnetic fields can enhance gravitational instability, Gammie (1996) argued against its validity based on the fact that radial magnetic field will be toroidally directed by shear on the time-scale $(q\Omega)^{-1}$. Thus, magnetic fields will destabilize axisymmetric gravitational modes only transiently, and become stabilizing long after $(q\Omega)^{-1}$, thus bringing this WKB analysis into question. An extension of this analysis shows that it is possible for non-axisymmetric modes to be destabilized by a toroidal magnetic field.[3] However, as a non-axisymmetric wavevector will eventually tend towards axisymmetry due to shear on the timescale $(q\Omega)^{-1}$ – $\mathbf{k} = (k_x + q\Omega t k_y)\hat{\mathbf{x}} + k_y\hat{\mathbf{y}}$, where k_x, k_y are the initial axisymmetric and non-axisymmetric wavenumbers (see Appendix C for a visual explanation.) – non-axisymmetric modes are only transiently unstable to a toroidal

[3]The stability analysis involving non-axisymmetric modes is more complicated as the wavevector is time-dependent. None the less, one can derive a set of equations [called the 'shearing sheet equations' by Goldreich & Lynden-Bell (1965), Julian & Toomre (1966), Elmegreen (1987), Gammie (1996), and Kim & Ostriker (2001)] that governs the amplitude of the perturbation, which can be solved in the same manner as one would solve an initial value problem. To characterize the strength of the instability, one then considers the maximum amplitude the density perturbations can grow to (a.k.a the 'responsiveness').

field[4]. Thus, we have a scenario where the wavevector becomes axisymmetric on the same (fast) time-scale as the field becoming toroidal, which is the configuration for which the magnetic field is a stabilizing influence.

We argue that this WKB analysis of axisymmetric modes can still, to a good extent, capture the growth structure in realistic scenarios based on the fact that radial magnetic fields lost to the toroidal direction due to shear can be continuously replenished by the MRI-dynamo on the dynamical time-scale, thus providing, in the mean-field sense, a roughly time-independent background field. In the weak vertical field case, the radial field is generally much weaker than the toroidal field. However, in the strong ($\beta \lesssim 10^2$) vertical field case, it has been shown that a relatively strong radial field with sustained polarity can be generated (Salvesen et al. 2016). We will characterize the strength and time-steadiness of this field in our simulations. The question is, can the MRI-dynamo produce a radial field strong and time-steady enough to trigger the CRMG instability? In the strong field limit it is likely that non-linear effects such as magnetic elevation will be active – would such effects inhibit fragmentation? We will clarify these issues in the following discussion. We note that a recent study by Kubli et al. (2023) found that significantly smaller clumps were formed when a magnetic field, amplified and maintained by a gravitoturbulent dynamo, was present. They noticed that most of the clumps were formed in low shear (small q) regions, where the wavevector and background magnetic field change in direction over a much longer time and the problem suggested by Gammie (1996) is assuaged. However, their focus was on protoplanetary discs, where MRI is less active and resistivity effects are strong. The gas in AGN discs tends to be more ionized within $\sim 10^3 r_g$, where MRI plays an important role in a dynamo. The shear parameter is most likely Keplerian ($q = 1.5$) at radii where self-gravity is important. Even if q were small at some distinct locations, it is unclear how the gas can be magnetized as MRI is likely suppressed for small q. Therefore, conditions in AGN discs could be completely different from protoplanetary discs, and our conclusions regarding the role of magnetic field could be different from Kubli et al. (2023).

5 RESULTS

In this section, we present results of our disc simulations. First, we outline general properties of the disc structure and discuss the α stresses (Reynolds, Maxwell, gravitational) found for simulations with different values of β_0. To clarify the role of magnetic fields in the gravitational stability of the system, we isolate various contributions to the magnetic budget and discuss the magnetic field structure of the disc, focusing on the in-disc field strength, orientation and time-steadiness as motivated by our discussion of the CRMG instability in Section 4. Having laid out the magnetic properties of the disc, we then discuss fragmentation in relation to the field structure and other disc parameters (e.g. the Toomre parameters). Using the dispersion relation equation (25), we show quantitatively how different aspects of the magnetic field conspire to promote or suppress fragmentation. In Table 1, we list the simulation parameters and transport quantities of the cases explored in this study.

5.1 Disc structure

In Fig. 5, we present time-series plots of the horizontally averaged density $\langle\rho\rangle_{xy}$ (left column), and the horizontally averaged radial field $\langle B_x\rangle_{xy}$ (middle column) and toroidal field $\langle B_y\rangle_{xy}$ (right column) for $\tau_{\rm cool} = 1$ and initial mid-plane plasma beta $\beta_0 = 10, 10^2, 10^3, 10^4, 10^5$ (increasing from top to bottom). Most of the test cases were run until $\Omega t = 300$, except the $\beta_0 = 10^5$ case, which was run until $\Omega t = 450$ due to the MRI saturating later. The black dashed lines in the left column indicate locations above and below the disc where the density is half the maximum, as a measure of the disc thickness. The colored contours in the middle and right columns indicate different levels of $\beta_x = 2\langle P_g\rangle_{xy}/\langle B_x\rangle^2_{xy}$ and $\beta_y = 2\langle P_g\rangle_{xy}/\langle B_y\rangle^2_{xy}$, respectively. As can be seen in the figure, stronger vertical magnetic field tends to puff up the disc, inducing strong outflows. Observe also that $\langle B_y\rangle_{xy}$ is generally stronger than $\langle B_x\rangle_{xy}$. This is consistent with the fact that any radial field generated from the MRI-dynamo is subjected to shear which winds it up in the toroidal direction[5]. Additionally, the polarities of the radial and toroidal magnetic field tend to be the same above and below the disc for the lower β_0 cases ($\beta_0 = 10, 10^2, 10^3$) in the saturated stage ($\Omega t \gtrsim 100$), while they reverse in polarity at the mid-plane for the high β_0 cases ($\beta_0 = 10^4, 10^5$). We do not observe quasi-periodic flip-flops of the magnetic field (butterfly structure) for the high β_0 cases ($\beta_0 = 10^4, 10^5$), as was observed in Bai & Stone (2013); Salvesen et al. (2016). A possible reason is that since cooling is proportional to the local thermal energy density in the cooling prescription (equation 11), cooling is weaker further from the disc mid-plane and the temperature rises with vertical height. This causes the entropy to increase with $|z|$ (left panel of Fig. 6), which by the Newcomb condition is stable against buoyant rise and interchange instabilities (Newcomb 1961; Riols & Latter 2018). This may prevent radial or toroidal flux from escaping vertically, which is key to the butterfly structure seen in Bai & Stone (2013) and Salvesen et al. (2016). The magnetic field profiles found in our simulations suggest the disc may be unstable to Parker (undular) modes except close to the mid-plane, according to the condition derived by Parker (1966) (right panel of Fig. 6)[6]. However, the instability condition derived by Parker (1966) comes from a global stability analysis and assumes an isothermal equilibrium profile whereas our simulated profile is not isothermal. Kim & Ryu (2001) also suggested that magnetic tension due to field randomness (which our turbulent discs exhibit) could reduce or completely suppress Parker modes. Thus it is unclear if Parker instability would be active. Finally, we note that the in-disc field B_x, B_y tapers off near the vertical boundaries as a result of the boundary conditions we use ($B_x = B_y = 0$).

In short, the disc thickness varies with the magnetic field in an expected way, and the magnetic fields in the low β_0 cases also agree with previous studies. However, the butterfly structure is absent in the high β_0 cases. This could be a result of the cooling prescription used, which seems to suppress buoyant rise of magnetic flux.

[4]Similar to axisymmetric CRMG modes, transient growth of non-axisymmetric modes in the presence of toroidal fields is faster for stronger fields (Elmegreen 1987). The problem is that this period of growth may be too short for clumps to deepen their gravitational potential well enough to become bound.

[5]An initially radial field $\mathbf{B}_0 = B_{x0}\hat{\mathbf{x}}$ subjected to shear $\mathbf{v} = -q\Omega x\hat{\mathbf{y}}$ does not remain radial. From the induction equation, $\partial\mathbf{B}/\partial t = -q\Omega B_{x0}\hat{\mathbf{y}}$, which gives $B_x = B_{x0}$, $B_y = -q\Omega B_{x0}t$, i.e. the field becomes toroidal with time.

[6]The condition for undular modes to be unstable in an isothermal equilibrium background is when the adiabatic index γ is less than some critical value $\gamma_{\rm c,u} = (1+\beta^{-1})^2/(1+1.5\beta^{-1})$, where $\beta = P_g/P_B$ is the plasma beta (Parker 1966).

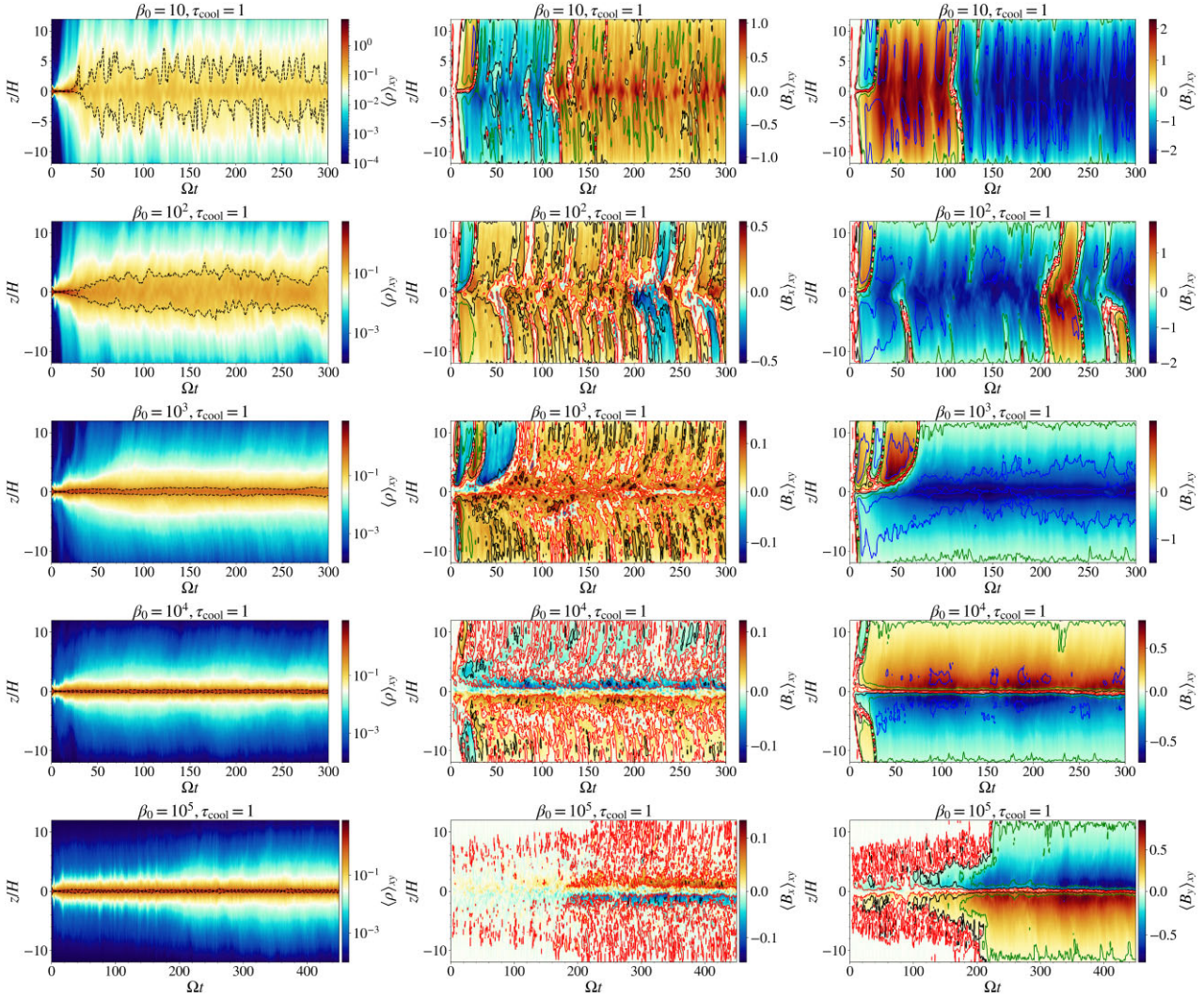

Figure 5. Time-series plot of $\langle\rho\rangle_{xy}$ (left column), $\langle B_x\rangle_{xy}$ (middle column), $\langle B_y\rangle_{xy}$ (right column), in code units. The initial mid-plane plasma beta β_0 increases through 10, 10^2, 10^3, 10^4, 10^5 from top to bottom, with the cooling time $\tau_{\rm cool} = 1$. In the left column, the black contour denotes the height for which the density is half the maximum at that particular time, i.e. the thickness of the disc. In the middle column, the contours denotes various levels of $\beta_x = 2\langle P_g\rangle_{xy}/\langle B_x\rangle^2_{xy}$, blue: $\beta_x = 0.1$, green: $\beta_x = 1$, black: $\beta_x = 10$, red: $\beta_x = 100$. The contours in the right column have the same meaning as in the middle column except now they denotes various levels of $\beta_y = 2\langle P_g\rangle_{xy}/\langle B_y\rangle^2_{xy}$.

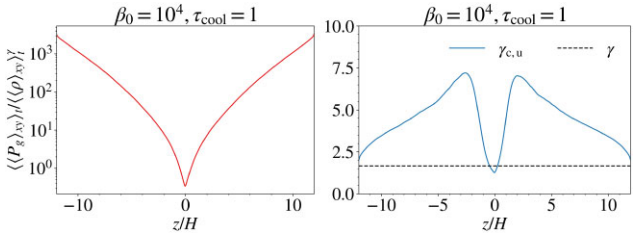

Figure 6. Left: Time-averaged, horizontally averaged entropy profile of the $\beta_0 = 10^4$, $\tau_{\rm cool} = 1$ case. Entropy here is measured by $\langle\langle P_g\rangle_{xy}\rangle_t/\langle\langle\rho\rangle_{xy}\rangle_t^\gamma$. Time-average is taken from $\Omega t = 100$–300. Right: Comparison of the adiabatic index used in the simulation ($\gamma = 5/3$, black dashed) against the critical γ for undular instability (blue solid line). $\gamma < \gamma_{\rm c,u}$ implies undular instability.

5.2 α stresses

We examine the various kinds of stresses in this section. In Fig. 7, we plot the volume averaged Reynolds (blue), Maxwell (red), and gravitational (green) stress against time. We plot the instantaneous $\langle\alpha_i\rangle_V$ values on the left column and the running-average $\langle\alpha_i\rangle_{V,\rm run}$ on the right for clarity. The running-average of a quantity at time t is the cumulative time-average of it up to t. In all cases explored, the Maxwell stress is the greatest, followed by the Reynolds stress and then the gravitational stress. In the saturated stage, the ratio of the Maxwell to Reynolds stress for the low β_0 cases (10, 10^2, 10^3) is roughly 3–4, consistent with previous stratified MRI simulations. For the high β_0 cases ($\beta_0 = 10^4$, 10^5), the onset of MRI is delayed (to $\Omega t \sim 100$ and 250 for the $\beta_0 = 10^4$, 10^5 cases, respectively). Taking the average over the last third of the simulation time span, we find that this ratio drops to roughly 1.5. The ratio of the gravitational to Reynolds stress exhibits an opposite trend, being $\ll 1$ in the low β_0 cases, but rising to ~ 0.5 for the high β_0 cases, hinting at strong suppression of GI in the low β_0 cases. This ordering of the stresses is observed in Riols & Latter (2018) as well, in their simulation with net vertical flux. The Maxwell stress α_M obtained in our simulations is slightly on the high side, but generally consistent with existing studies in the strong cooling regime for low β_0 cases (e.g. Gammie

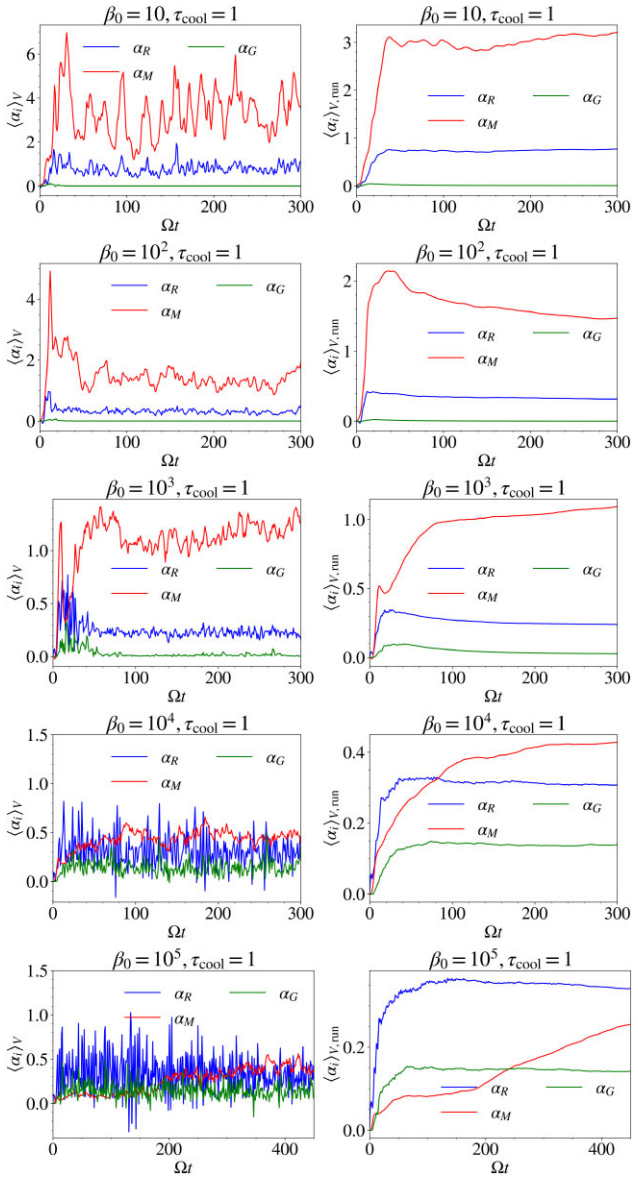

Figure 7. Volume averaged Reynolds (blue), Maxwell (red) and gravitational (green) stresses as a function of time for various β_0 cases. Left column: The instantaneous $\langle \alpha_i \rangle_V$ at each time. Right column: The running-average of $\langle \alpha_i \rangle_V$.

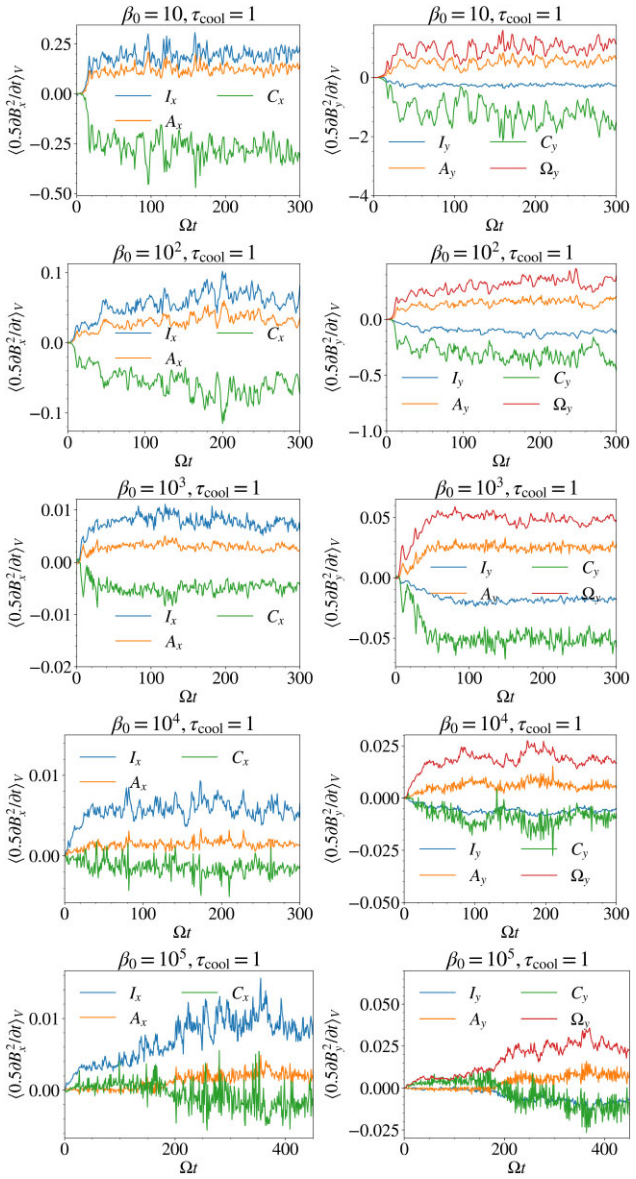

Figure 8. Decomposition for $\partial B_x^2/\partial t$ (left column) and $\partial B_y^2/\partial t$ (right column), each curve denoting the volume average of a term in the decomposition (equation 28), against time for various β_0 cases.

2001; Salvesen et al. 2016). However, the stresses in the high β_0 cases are orders of magnitude higher than standard MRI calculations. α_M reaches up to ~ 3 for $\beta_0 = 10$, and ~ 0.3 for $\beta_0 = 10^5$, showing a decreasing trend with respect to β_0. This decreasing trend is very weak, with a dependence $\sim \beta_0^{-1/4}$, compared with the $\sim \beta^{-1/2}$ dependence obtained in previous simulations (Salvesen et al. 2016). Note that there is no self-gravity in Salvesen et al. (2016); This is suggestive of gravitoturbulence at play boosting the stresses in the high β_0 cases.

To aid our understanding of the growth and sustenance of the magnetic field, we decompose the magnetic budget into various contributions, as in Riols & Latter (2018), and plot them in Fig. 8. From the induction equation, we obtain

$$\frac{1}{2}\frac{\partial B_i^2}{\partial t} = I_i + A_i + C_i + \Omega_i, \tag{28}$$

where $I_i = B_i B_j \, \partial \delta v_i / \partial x_j$ denotes the 'stretching' term, $A_i = -B_i \delta v_j \, \partial B_i / \partial x_j$ is the advection term, $C_i = -B_i^2 \nabla \cdot \delta \mathbf{v}$ is the compression term, and $\Omega_i = q\Omega(x B_i \, \partial B_i / \partial y - B_i B_x)\delta_{iy}$ is the Ω-effect (linear stretching by shear). Note that summation is implied for j but not i in equation (28), and $\delta \mathbf{v} = \mathbf{v} + q\Omega x \hat{\mathbf{y}}$ is the fluctuation velocity. In practice, the first term of the Ω contribution ($q\Omega x B_i \, \partial B_i / \partial y$) is negligible, so $\Omega_i \approx -q\Omega B_i B_x$ effectively. We note that the stretching term I_x is the dominant contribution to the radial field, while the Ω term (stretching by shear) is the dominant contribution to the toroidal field. These results are consistent with Riols & Latter (2018). Unlike their findings, advection (A_i) and compression (C_i) terms are not negligible in our simulations, especially for low β_0 cases, where A_i, C_i can be comparable in magnitude to the dominant term. Advection effects (A_i) generally supplement field generation while compression effects (C_i) are the dominant counter-balance terms for the magnetic field budget in all cases. An examination of the

constituent terms for A_i, C_i (not shown here) shows that at low β_0, the contributions from terms involving v_z dominate, leading to exceptionally large magnitudes of A_i, C_i. In high β_0 cases where v_z is small, A_i, C_i are weaker. While this suggests vertical expansion and advection by a magnetically driven wind at low β_0 could be important to field generation, note that A_i and C_i are anticorrelated. We know for a fact that the vertical wind speed generally increases with height $|z|$ while the magnetic field generally decreases with $|z|$. Suppose

$$v_z(z) \propto B_i^{-p}(z), \tag{29}$$

where $p > 0$ generally. After some manipulation, we find that

$$-B_i^2 \frac{\partial v_z}{\partial z} = p v_z \frac{\partial}{\partial z}\left(\frac{B_i^2}{2}\right). \tag{30}$$

Since the terms involving v_z dominate the contributions to A_i, C_i when the wind is strong, equation (30) implies

$$C_i \approx -pA_i. \tag{31}$$

That is, if $p = 1$, then the advective term cancels the compression term. If $p < 1$ and A_i remains positive, the combined advective and compression contributions from the wind then contribute positively to magnetic field generation.

Riols & Latter (2018) found in several zero-net-flux simulations with self-gravity and strong cooling ($\tau_{\rm cool} \lesssim 5$) that magnetic field is generated mostly by a gravitoturbulent dynamo, as demonstrated by high levels of gravitational stress that are comparable to or exceed the Reynolds and Maxwell stresses. They also noticed a change in the location of field generation from $|z| \sim H$ (above and below the disc) in pure MRI to $|z| \sim 0$ (within the disc) in gravitoturbulent dynamos. The subdominant levels of gravitational stress observed in our low β_0 simulations seem to suggest against a gravitoturbulent dynamo at play in those cases. However, in the high β_0 cases, the relatively high levels of gravitational stresses together with the higher stresses compared to standard MRI calculations is suggestive of a gravitoturbulent dynamo at play, consistent with Riols & Latter (2018). Unlike in pure MRI (no cooling or self-gravity), field generation occurs mostly at $z \sim 0$ in our simulations. We attribute this to cooling suppressing the buoyant rise of disc gas. We conclude that MRI-generated turbulence is still responsible for the dynamo process needed for field generation in our low β_0 simulations, while there could be mixed contributions from MRI and gravitoturbulence in the high β_0 cases. In a simulation performed by Riols & Latter (2018) with net flux and a moderately strong initial field ($\beta_0 \approx 225$), it was found that the gravitational stress is the most subdominant stress, consistent with our low β_0 test cases.

Magnetic field generation in set-ups with self-gravity and cooling is a profound subject warranting a separate study. For our purposes, we simply note that evidence does not seem to support self-gravity being responsible for the dynamo process in our low β_0 simulations, but could be conducive to such due to fragmentation in the high β_0 cases. We also observe that flux-tube-stretching I_x is the dominant contribution to the radial field which, when fed into flows with shear, contributes to most of the toroidal field generated through the shearing term Ω_i.

5.3 Magnetic field structure

In this section, we examine the magnetic fields in our simulations. The first thing we would like to point out is that the strength of the radial and vertical fields varies with scale. The meaning of this is illustrated in Fig. 9, which shows the window-averaged,

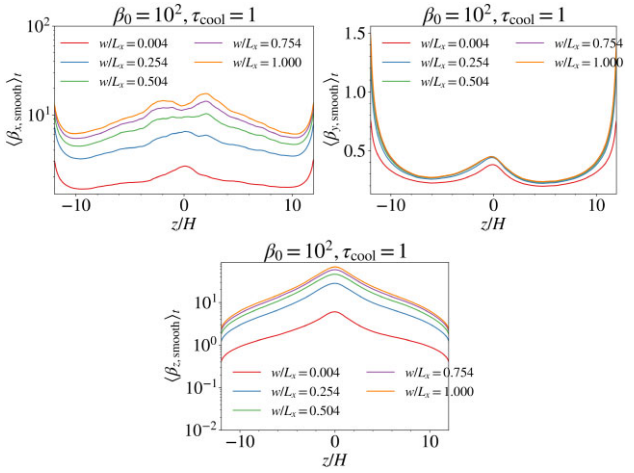

Figure 9. Top left: Window-averaged, time-averaged plasma beta of the radial field defined by $\langle\beta_{x,\rm smooth}\rangle_t = 2\langle\langle\bar{P}_{g,w}\rangle_{xy}\rangle_t / \langle\langle\bar{B}^2_{x,w}\rangle_{xy}\rangle_t$. Top right: Window-averaged, time-averaged plasma beta of the toroidal field $\langle\beta_{x,\rm smooth}\rangle_t = 2\langle\langle\bar{P}_{g,w}\rangle_{xy}\rangle_t / \langle\langle\bar{B}^2_{y,w}\rangle_{xy}\rangle_t$. Bottom: Window-averaged, time-averaged plasma beta of the vertical field $\langle\beta_{z,\rm smooth}\rangle_t = 2\langle\langle\bar{P}_{g,w}\rangle_{xy}\rangle_t / \langle\langle\bar{B}^2_{z,w}\rangle_{xy}\rangle_t$. Various window lengths w are displayed. The case displayed is $\beta_0 = 10^2$, $\beta_{\rm cool} = 1$. Time-average is taken from $\Omega t = 100 - 300$.

time-averaged plasma beta parameter corresponding to the radial field $\langle\beta_{x,\rm smooth}\rangle_t = 2\langle\langle\bar{P}_{g,w}\rangle_{xy}\rangle_t / \langle\langle\bar{B}^2_{x,w}\rangle_{xy}\rangle_t$ (top left), toroidal field $\langle\beta_{y,\rm smooth}\rangle_t = 2\langle\langle\bar{P}_{g,w}\rangle_{xy}\rangle_t / \langle\langle\bar{B}^2_{y,w}\rangle_{xy}\rangle_t$ (top right), and vertical field $\langle\beta_{z,\rm smooth}\rangle_t = 2\langle\langle\bar{P}_{g,w}\rangle_{xy}\rangle_t / \langle\langle\bar{B}^2_{z,w}\rangle_{xy}\rangle_t$ (bottom) for different window lengths, where the time average is taken from $\Omega t = 100$–300. The displayed case is $\beta_0 = 10^2$, $\tau_{\rm cool} = 1$. The meaning of window-average, and the notation $\bar{X}_w$, is explained in Section 3. Briefly, it is a smoothing operation in the x, y-direction, with w being the smoothing window. By performing such smoothing operations, we are essentially removing contributions from modes with wavenumbers $k_x w, k_y w > 1$. A clear difference between the top right panel and the rest of Fig. 9 is that $\beta_{x,\rm smooth}, \beta_{z,\rm smooth}$ are sensitive to the window length chosen, while $\beta_{y,\rm smooth}$ is insensitive to it. This means there is a lot of small scale structure in the radial and vertical field while the azimuthal field structure consists mostly of a single, large scale field. The difference in $\beta_{x,\rm smooth}, \beta_{z,\rm smooth}$ when one includes all small scale modes[7] (the smallest window width $w/L_x = 0.004$) compared to when one includes only the domain-sized mode (the largest window width $w/L_x = 1$) can be an order of magnitude for the case shown. In this section, when discussing quantities related to the field, we will display only window-averaged results with window lengths $w/L_x = 0.004$ and $w/L_x = 1$ (or as specified) to reduce clutter, representing results including the full spectrum and just the large-scale, respectively.

The second thing we would like to point out is that the magnetization in the non-linear stage generally increases with decreasing β_0, but not necessarily in a monotonic manner for some field components. In Fig. 10, we plot in the left column the window-averaged, time-averaged profiles of the radial field plasma beta $\langle\beta_{x,\rm smooth}\rangle_t$ (top left), the toroidal field plasma beta $\langle\beta_{y,\rm smooth}\rangle_t$ (second row left), the vertical field plasma beta $\langle\beta_{z,\rm smooth}\rangle_t$ (third row left), and the relative radial field strength $\langle b_{x,\rm smooth}\rangle_t = [\langle\langle\bar{B}^2_{x,w}\rangle_{xy}\rangle_t / (\langle\langle\bar{B}^2_{x,w}\rangle_{xy}\rangle_t + \langle\langle\bar{B}^2_{y,w}\rangle_{xy}\rangle_t)]^{1/2}$ (bottom left) for various β_0, with $w/L_x = 1$ as the

[7] β depends inversely on field strength so a low value for the small window means a lot more mangetic energy density.

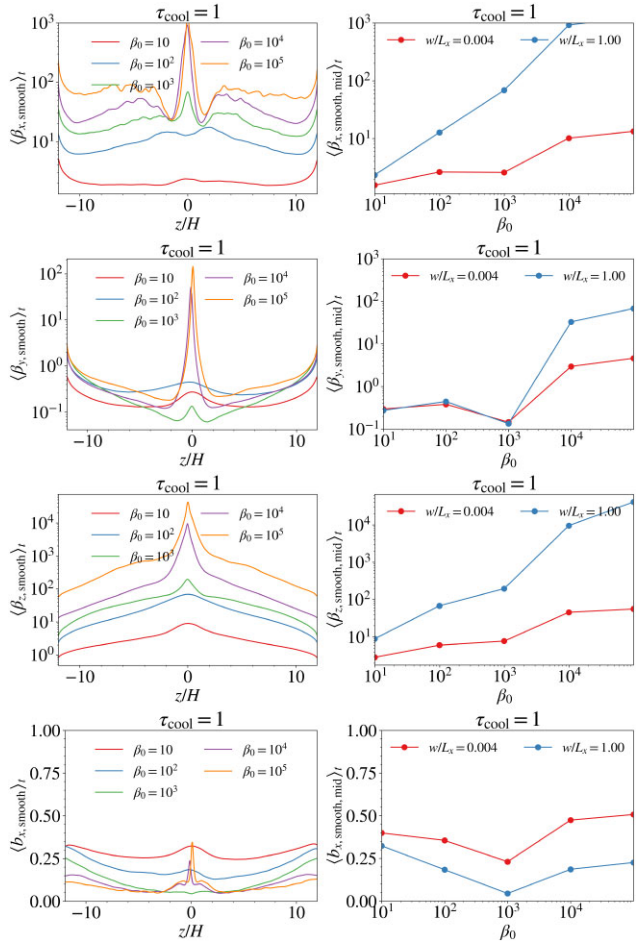

Figure 10. Left column: Window-averaged, time-averaged profiles of the radial field plasma beta $\langle\beta_{x,\rm smooth}\rangle_t = 2\langle\langle\bar{P}_{g,w}\rangle_{xy}\rangle_t/\langle\langle\bar{B}^2_{x,w}\rangle_{xy}\rangle_t$ (top left), the toroidal field plasma beta $\langle\beta_{y,\rm smooth}\rangle_t = 2\langle\langle\bar{P}_{g,w}\rangle_{xy}\rangle_t/\langle\langle\bar{B}^2_{y,w}\rangle_{xy}\rangle_t$ (second row left), the vertical field plasma beta $\langle\beta_{z,\rm smooth}\rangle_t = 2\langle\langle\bar{P}_{g,w}\rangle_{xy}\rangle_t/\langle\langle\bar{B}^2_{z,w}\rangle_{xy}\rangle_t$ (third row left), and the relative radial field strength $\langle b_{x,\rm smooth}\rangle_t = [\langle\langle\bar{B}^2_{x,w}\rangle_{xy}\rangle_t/(\langle\langle\bar{B}^2_{x,w}\rangle_{xy}\rangle_t + \langle\langle\bar{B}^2_{y,w}\rangle_{xy}\rangle_t)]^{1/2}$ (bottom left) for various β_0, with $w/L_x = 1$ as the window length. Right column: Plot of $\langle\beta_{x,\rm smooth,mid}\rangle_t$ (top right), $\langle\beta_{y,\rm smooth,mid}\rangle_t$ (second row right), $\langle\beta_{z,\rm smooth,mid}\rangle_t$ (third row right) and $\langle b_{x,\rm smooth,mid}\rangle_t$ (bottom right), where the subscript 'mid' denotes values taken at $z = 0$, as a function of β_0, for two window lengths: $w/L_x = 0.004$ (red line), $w/L_x = 1$ (blue line). The cases displayed have $\tau_{\rm cool} = 1$. Time-average is taken from $\Omega t = 100 - 300$ for the $\beta_0 \leq 10^4$ cases and from $\Omega t = 250 - 450$ for the $\beta_0 = 10^5$ case.

window length. We note that the magnetic field is typically stronger above and below the disc, with the disc mid-plane being the least magnetically dominant[8]. The mid-plane magnetic field strength is particularly weak for the high β_0 cases ($\beta_0 = 10^4, 10^5$), reflecting field reversals seen in Fig. 5 at $z = 0$. The low β_0 cases $\beta_0 = 10, 10^2$ do not suffer such a flip in polarity at the mid-plane, and are able to maintain field strength at the mid-plane that is comparable to the corona. In the right column of Fig. 10, we pick out the values of $\langle\beta_{x,\rm smooth}\rangle_t$, $\langle\beta_{y,\rm smooth}\rangle_t$, $\langle\beta_{z,\rm smooth}\rangle_t$, and $\langle b_{x,\rm smooth}\rangle_t$ at $z = 0$ (hence the subscript 'mid') and plot them against β_0. The mid-plane is particularly relevant as fragmentation happens mostly there. We observe that the mid-plane radial plasma beta $\langle\beta_{x,\rm smooth,mid}\rangle_t$ increases monotonically with respect to β_0 regardless of the window length chosen (i.e. scale), with the large-scale beta dropping from $\sim 10^3$ for $\beta_0 = 10^5$ to ~ 1 for $\beta_0 = 10$. The toroidal plasma beta $\langle\beta_{y,\rm smooth,mid}\rangle_t$ does not drop monotonically with respect to β_0. It exhibits an asymmetric U-shape pattern, with the minimum located at $\beta_0 = 10^3$, at which the value is ~ 0.1. The two ends of the U-shaped pattern have values of $\sim 10^2$ and ~ 0.5 at $\beta_0 = 10^5$, 10 respectively. Similar to the radial plasma beta, the vertical plasma beta $\langle\beta_{z,\rm smooth,mid}\rangle_t$ again decreases monotonically with respect to β_0, with the large-scale field dropping from $\sim 10^5$ for $\beta_0 = 10^5$ to ~ 10 for $\beta_0 = 10$, just as in the initial set-up, while the small-scale components are significantly stronger, hovering between $5 - 15$. We know that MRI does not modify the mean vertical field much, so this implies that the averaged mid-plane gas pressure remains more or less the same as the initial value despite the thermodynamical changes throughout the simulation. The relative radial field strength $\langle b_{x,\rm smooth,mid}\rangle_t$ exhibits the same U-shaped trend as $\beta_{y,\rm smooth,mid}$, with a minimum located at $\beta_0 = 10^3$ in which the value is close to zero, implying the in-disc field is mostly toroidal. The two ends of the U-shaped pattern have $\langle b_{x,\rm smooth,mid}\rangle_t$ values between 0.25 to 0.5 depending on the scale, indicating the toroidal field component is still dominant, but the radial field component is non-negligible.

In Fig. 11, we plot the window-averaged radial field plasma beta $\beta_{x,\rm smooth,mid} = 2\langle\bar{P}_{g,w,\rm mid}\rangle_{xy}/\langle\bar{B}^2_{x,w,\rm mid}\rangle_{xy}$ (left), toroidal field plasma beta $\beta_{x,\rm smooth,mid} = 2\langle\bar{P}_{g,w,\rm mid}\rangle_{xy}/\langle\bar{B}^2_{y,w,\rm mid}\rangle_{xy}$ (middle), and the relative radial field strength $b_{x,\rm smooth,mid} = [\langle\bar{B}^2_{x,w,\rm mid}\rangle_{xy}/(\langle\bar{B}^2_{y,w,\rm mid}\rangle_{xy} + \langle\bar{B}^2_{y,w,\rm mid}\rangle_{xy})]^{1/2}$ (right) at the mid-plane, using a window length of $w/L_x = 1$ (i.e. large scale field), as a function of time. We note that rapid fluctuations in β_x, β_y are observed for the high $\beta_0 = 10^4, 10^5$ cases. Fluctuations can still be seen in β_x, β_y for the lower β_0 cases, but they are less rapid than their high β_0 counterparts. In the top row of Fig. 12, we characterize the magnitude of the fluctuations using the quantities $\sigma(\log\langle\beta_i\rangle^{\rm smooth}_{xy})$ and $\sigma(\langle b_x\rangle^{\rm smooth}_{xy})$, which are the standard deviation of the logarithm (base 10) of $\beta_{i,\rm smooth,mid}$ ($i = x, y$) (left panel) and that of $b_{x,\rm smooth,mid}$ (right). The standard deviations are taken over $\Omega t = 100 - 300$ (for $\beta_0 \neq 10^5$) and over $\Omega t = 250 - 450$ for $\beta_0 = 10^5$. The magnitude of the fluctuations in β_x, β_y are quite similar across different β_0 cases, with $\Delta\log\beta_i \sim 0.35 - 0.45$, except for the $\beta_0 = 10^3$ case, in which β_y is particularly steady. This implies that the large-scale β_x, β_y at the mid-plane varies typically by 0.35–0.45 dex (i.e. less than an order of magnitude). As observed in the top right panel, b_x typically varies by $\Delta b_x \sim 0.1 - 0.15$, except for the $\beta_0 = 10^3$ case, which as a low value of ~ 0.01. Depending on the local conditions, such fluctuations could either mean insignificant or appreciable change in the growth rates. As we shall see in Section 5.4.1 (also Fig. 16), the resultant fluctuations in the growth rates are modest.

In the bottom row of Fig. 12, we display the fraction of power contained in the low frequency part (with period $> 10\Omega^{-1}$) of the temporal spectrum of $\beta_{x,\rm smooth,mid}$, $\beta_{y,\rm smooth,mid}$, $b_{x,\rm smooth,mid}$. We calculate this by

$$P(X) \equiv \frac{\int_0^{\omega(T>10\Omega^{-1})} \left|\tilde{X}\right| {\rm d}\omega}{\int_0^{\infty} \left|\tilde{X}\right| {\rm d}\omega}, \tag{32}$$

where $\tilde{X}$ is the temporal FFT of the quantity X. The bottom left plot shows that roughly 40 per cent of the power of $\beta_{x,\rm smooth,mid}$ is contained in the low frequency part, and $40 - 60$ per cent for $\beta_{y,\rm smooth,mid}$. The radial field contribution b_x is more time-steady, with around 70 per cent contained in the low frequency part for the low β_0 cases, dwindling to 50 per cent for the high β_0 cases. These plots imply that while the WKB analysis is, strictly speaking, not

[8]The upward drift in β_x, β_y at large $|z|$ is due to the boundary conditions used, for which B_x, $B_y = 0$ at the z-boundaries.

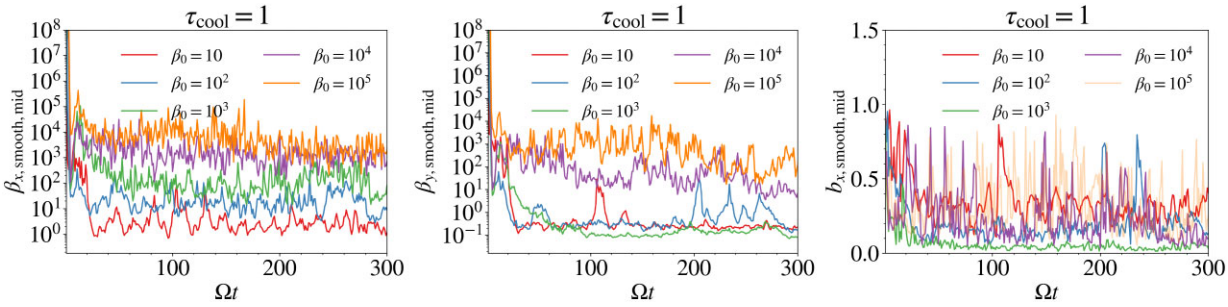

Figure 11. Window-averaged radial field plasma beta $\beta_{x,\rm smooth,mid} = 2\langle \bar{P}_{g,w,\rm mid}\rangle_{xy}/\langle \hat{B}^2_{x,w,\rm mid}\rangle_{xy}$ (left), toroidal field plasma beta $\beta_{y,\rm smooth,mid} = 2\langle \bar{P}_{g,w,\rm mid}\rangle_{xy}/\langle \hat{B}^2_{y,w,\rm mid}\rangle_{xy}$ (middle), and relative radial field strength $b_{x,\rm smooth,mid} = [\langle \bar{B}^2_{x,w,\rm mid}\rangle_{xy}/(\langle \bar{B}^2_{x,w,\rm mid}\rangle_{xy} + \langle \bar{B}^2_{y,w,\rm mid}\rangle_{xy})]^{1/2}$ at the mid-plane as a function of time for various initial mid-plane plasma beta β_0. The cooling strength for the displayed cases is $\tau_{\rm cool} = 1$. The window-length used for the window average is $w/L_x = 1$.

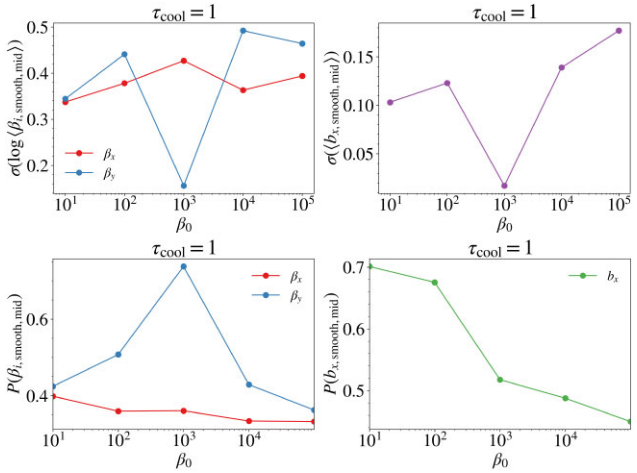

Figure 12. Top left: Fluctuations of the window-averaged plasma betas $\beta_{x,\rm smooth,mid}$ (red), $\beta_{y,\rm smooth,mid}$ (blue) at the mid-plane for different β_0 cases, measured in terms of the standard deviation of the logarithm (base 10) of the respective window-averaged betas β_i. Top right: same as the left panel but for the relative radial field contribution b_x. Bottom row: Fraction of power contained in temporal frequencies with period longer than $10\Omega^{-1}$ for $\beta_{x,\rm smooth,mid}$, $\beta_{y,\rm smooth,mid}$ (left) and $b_{x,\rm smooth,mid}$ (right).

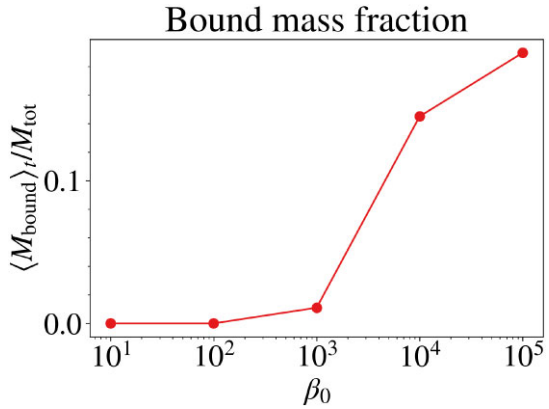

Figure 13. Time-averaged bound mass fraction $\langle M_{\rm bound}\rangle_t/M_{\rm tot}$, where $\langle M_{\rm bound}\rangle_t$ is the time averaged bound mass within the box (i.e. located within TBRs, as defined in equation 24), and $M_{\rm tot}$ is the total mass within the box, which is kept constant in our set-up. This is plotted against the initial mid-plane plasma beta β_0. Time-average is taken from $\Omega t = 100 - 300$, except for the $\beta_0 = 10^5$ case, for which time-average is taken from Ωt = 250–450.

valid due to presence of high frequency fluctuations (with fluctuation periods comparable or shorter than the growth time), it remains an insightful tool to understand the growth of GI modes in this complex environment since there is substantial power in the low frequency parts. In particular, b_x, which controls whether magnetic field destabilizes axisymmetric CRMG modes (Fig. 4), is highly time-steady in the low β_0 cases.

In summary, there are several noteworthy points regarding the magnetic field structure. First, the radial and vertical fields are multiscaled, with grid size structures as well as domain-sized mean field, while the toroidal field is mostly large-scaled. Secondly, the magnetization of the disc in the nonlinear stage generally increases with decreasing β_0, but not necessarily in a monotonic manner. Specifically, the gas is the most magnetically dominated and toroidally directed for $\beta_0 = 10^3$, while the radial field contribution increases for $\beta_0 < 10^3$. Overall, the low β_0 (10, 10^2, 10^3) cases are considerably more magnetically dominated at the mid-plane than the high β_0 cases. Thirdly, the large-scale magnetic field at the mid-plane can be considered approximately time-steady, with fluctuations in β_x, β_y of order $\sim 0.35 - 0.45$ dex – which only has a modest effect on the growth rates – and more than 40 per cent of the power contained in the low frequency part of the temporal spectrum. Taken together, these observations suggest that MRI is able to produce steady radial and toroidal field of appreciable magnitude, particularly in the low β_0 cases.

5.4 Disc fragmentation

Using the clump identification algorithm outlined in Section 3.1, we identified clumps satisfying equation (24) within the time period $\Omega t = 100 - 300$ and collected their properties (e.g. mass, size, location, etc.). As Athena++ is an Eulerian code, we cannot trace the evolution of the clumps as one could with an SPH-based code (e.g. Gizmo, Hopkins 2015), as in Kubli et al. (2023). Therefore, we focus on the time-averaged properties of the clumps, in which we identify clumps and collect their properties for every output file within $\Omega t = 100 - 300$ (or $\Omega t = 250 - 450$ for the $\beta_0 = 10^5$ case), and take the average of these properties over the files we read. To calculate the average fraction of bounded mass in the box, we first sum over the fraction of bounded mass in each output snapshot, then divide this by the number of snapshots we scanned through.

In Fig. 13, we show the averaged bound mass fraction as a function of β_0. We note that the bound mass fraction decreases for stronger initial fields, dropping roughly a factor of 10 from $\beta_0 = 10^4$ to $\beta_0 =$

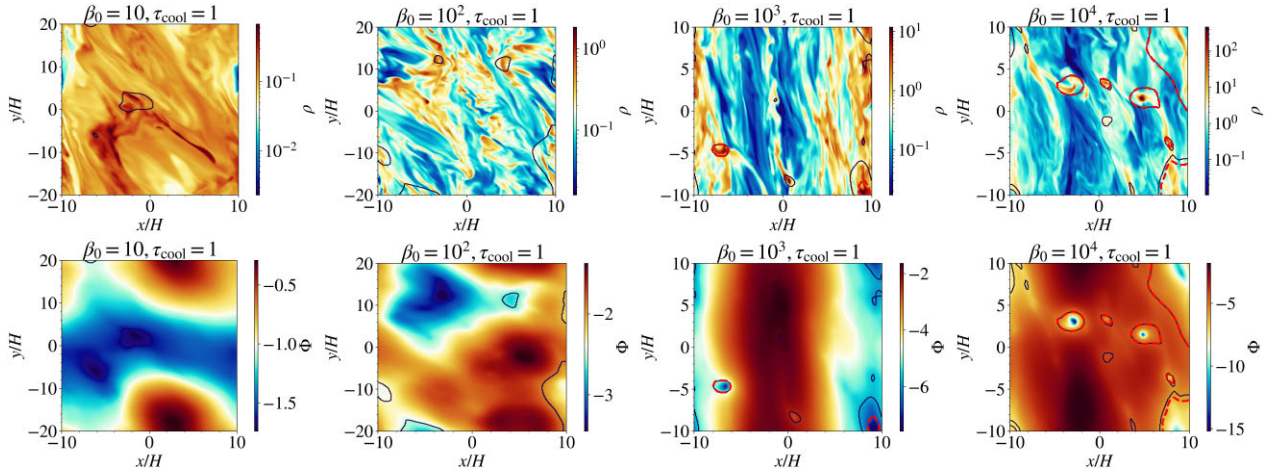

Figure 14. Snapshots of the mid-plane ρ (top row) and Φ (bottom row) taken at $\Omega t = 200$ with contours overlaid to indicate clumps identified. From left to right, $\beta_0 = 10, 10^2, 10^3, 10^4$, $\tau_{\rm cool} = 1$. Black contours: Gravitational Binding Region (GBR, i.e. isolated region that is gravitationally bound); Red-dashed contours: Total Binding Region (TBR, i.e. isolated region that is bound when thermal, kinetic and magnetic pressure support are taken in account.).

10^3, and no clumps were identified for $\beta_0 = 10, 10^2$. This strongly suggests that GI is suppressed for low β_0 cases. In Fig. 14, we display selected snapshots of the mid-plane density and gravitational potential with GBR (black) and TBR (red) contours overlaid. Clearly, the number of clumps decreases as β_0 decreases.

5.4.1 *Mid-plane properties and magnetic elevation*

Despite appreciable radial field contribution b_x in some low β_0 cases and the decrease in plasma beta β at the mid-plane going from $\beta_0 = 10^5$ to 10 (Fig. 10), we observe no uptick in fragmentation (in terms of the bound mass fraction), which seems to contradict expectation from linear theory. This is because the CRMG instability growth rate depends not just on b_x and β, but also on other parameters which may adversely impact the growth rate when a strong magnetic field is present. In this section, we investigate the conditions at the mid-plane to address why fragmentation/GI is suppressed for the low β_0 ($\leq 10^3$) cases.

In the top row of Fig. 15, we plot the horizontally averaged, time-averaged mid-plane density, thermal sound speed (top left) and plasma beta (top right) as a function of β_0. There are two note-worthy points in this figure. First, the density at the mid-plane decreases by over an order of magnitude from $\beta_0 = 10^5$ to $\beta_0 = 10$. Secondly, the mid-plane magnetic field becomes dominant for $\beta_0 \leq 10^3$. These two points indicate clearly that the disc is magnetically elevated for $\beta_0 \leq 10^3$ (Begelman & Silk 2017). We also observe an increase in the sound speed going to lower β_0, indicating an enhanced thermal scale height at the mid-plane. To quantify the extent to which the increase in the vertical scale height is due to magnetic elevation versus that due to increase in gas temperature, we list for different β_0 cases in Table 2 the scale height measured from the time and horizontal-averaged density profile $\hat{H}$, defined by the height at which the density drops by an e-fold ($\rho_{\rm max} e^{-1}$), and also the time and horizontal-averaged mid-plane gas sound speed $\langle c_{s,\rm mid} \rangle_t$. Note that $\hat{H}$ is defined differently from the usual definition of thermal scale-height c_s/Ω, thus we need to calibrate $\hat{H}$ using a reference point to interpret our numbers. Focusing on the $\beta_0 = 10^5$ case, for which magnetic elevation can be considered absent, $\hat{H} = 0.352H$ (where H is the initial mid-plane thermal scale-height). The time-averaged mid-plane thermal scale-height $\langle c_{s,\rm mid} \rangle_t / \Omega = 1.05H$. Going from $\beta_0 = 10^5$ to $\beta_0 = 10$, $\hat{H}$ increases by roughly 16 times while $\langle c_{s\rm mid} \rangle_t / \Omega$ increases only by 2.8 times. We can reasonably infer that while the increase in gas temperature contributes an increase of 2.8 to the vertical scale height, the combined thermal plus magnetic pressure led to an increase of 16 times, indicating the dominant effect of magnetic elevation[9].

The gravitational instability growth rate depends sensitively on the Toomre parameter $Q_{\rm T}$ (discussed in Section 4.1). The bottom row of Fig. 15 shows that the change in mid-plane properties result in larger $Q_{\rm T}$, which tends to lower the instability growth rate. The proxy Toomre parameter Q is also significantly increased. Similarly, the magnetized Toomre parameter $Q_{{\rm T},B}$ increases for lower β_0, rising way above 1, the stability threshold for magneto-Jeans mode. In Table 2, we list some time and horizontally averaged mid-plane properties. Using the mid-plane quantities extracted from each output snapshot, we calculate the most unstable axisymmetric CRMG growth rate and the corresponding wavenumber at the mid-plane for all the cases using the dispersion relation equation (C21)[10], plotting them as a function of time in the top panels of Fig. 16. We also plot, in the same figure, the time-averaged growth rate and the associated wavenumber as a function of β_0. This figure shows that the axisymmetric CRMG growth rate decreases by close to an order of magnitude as β_0 decreases from 10^5 to 10, indicating suppression of GI due to the different mid-plane properties in the low β_0 cases, consistent with the lack of fragmentation in those cases. The most unstable wavelengths are also much shorter in the low $\beta_0 < 10^3$ cases ($k_{x,\rm max} \sim 1.5\Omega/c_s$) than the high β_0 cases ($k_{x,\rm max} \approx 0$); however, we are unable to confirm this as as we did not capture any clumps in the $\beta_0 = 10, 10^2$ cases and only a few in the $\beta_0 = 10^3$ case, insufficient for a statistical analysis.

[9]We did not define a magnetic scale height $\langle v_{A,\rm mid} \rangle_t / \Omega$ in the same manner as thermal scale height because the magnetic pressure at the mid-plane is substantially weaker than above and below the disc, so it is unclear how this number would reflect the actual increase in vertical scale-height due to magnetic fields.

[10]Note that we are using the axisymmetric CRMG dispersion relation assuming a uniform background for this calculation as it is a more appropriate approximation for an elevated disc at the mid-plane.

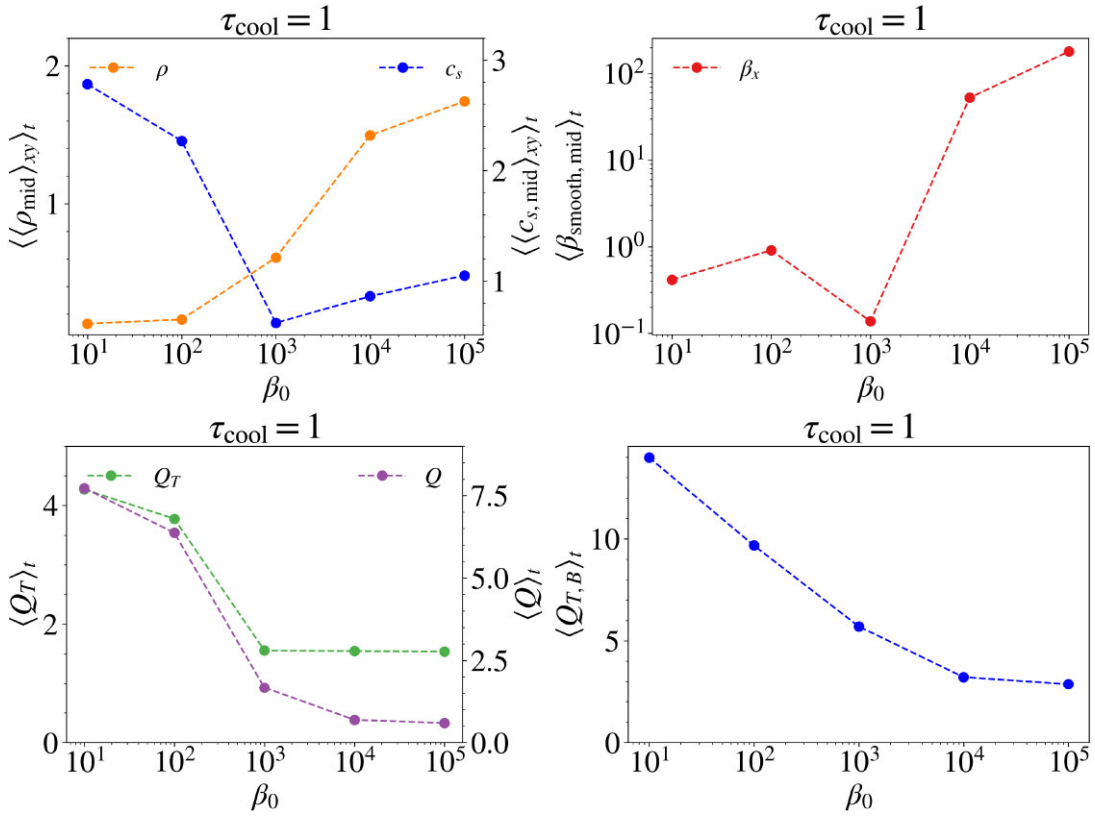

Figure 15. Horizontally averaged, time-averaged mid-plane density (top left, orange), thermal sound speed (top left, blue), window-averaged plasma beta (top right, with a smoothing length of L_x), Toomre parameter $Q_{\rm T}$ (bottom left, green), proxy Toomre parameter Q (bottom left, purple) and magnetized Toomre parameter (bottom right) for different β_0. Time-average is taken from $\Omega t = 100$–300, except for the $\beta_0 = 10^5$ case, which is taken from $\Omega t = 250$–450.

Table 2. Mid-plane quantities for the different β_0 cases. Note that we have moved the 'smooth' subscript to the superscript position for β, b_x to avoid overstretching the table. We are not introducing new variables. $\hat{H}$ in the rightmost column is the scale height (in units of initial mid-plane scale height H) measured from the time-averaged density profile (defined by the height at which the density drops by an e-fold $\rho_{\rm max}e^{-1}$).

β_0	$\langle\beta^{\rm smooth}_{\rm mid}\rangle_t$	$\langle c_{s,\rm mid}\rangle_t$	$\langle Q\rangle_t$	$\langle b^{\rm smooth}_{x,\rm mid}\rangle_t$	$\hat{H}/H$
10	0.437	2.78	7.73	0.324	5.66
10^2	0.913	2.27	6.37	0.196	3.91
10^3	0.131	0.622	1.67	0.041	0.773
10^4	52.679	0.863	0.688	0.198	0.305
10^5	179.584	1.05	0.591	0.273	0.352

In the low β_0 $(10, 10^2)$ cases, the simple WKB linear analysis predicts a growth rate of $\gamma \sim 0.1 - 0.2\Omega$, corresponding to an e-folding time of $\sim 30 - 60\Omega^{-1}$. Such an increase in growth time results in a drastic decrease in fragmentation and further lowers the validity of the WKB analysis in that scenario. It is unlikely that perturbations would be able to sustain exponential growth over such a long e-folding time; we suspect that only weak transient growth is possible before background conditions check further growth or even damp it.

Thus, the potential increase in growth rate due to increased magnetic field (decreased β) is negated by magnetic elevation in the low β_0 cases. The disc mid-plane becomes magnetic pressure-dominated, making the gas more rarefied (i.e. lower density) and contributing to increased Toomre parameter which drastically lowers the CRMG growth rate.

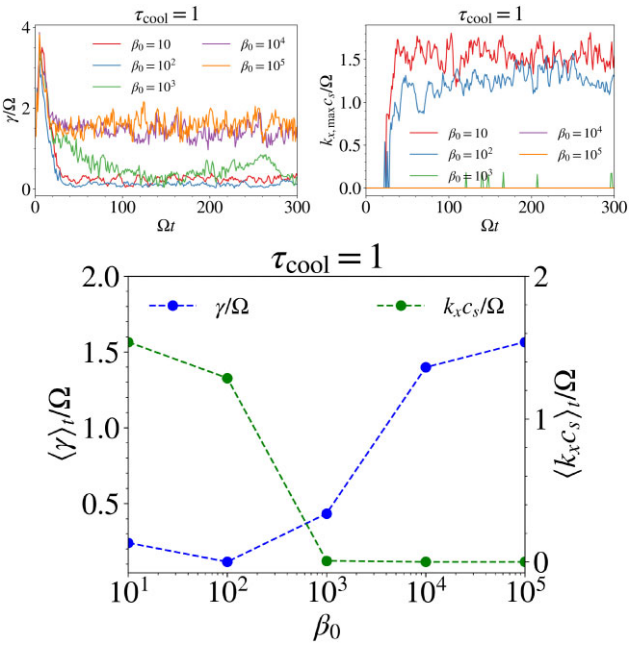

Figure 16. The CRMG growth rate (top left) and the corresponding wavenumber (top right) of axisymmetric modes against time for various β_0, calculated using the horizontally averaged mid-plane properties. Bottom: the growth rates and the associated wavenumbers calculated by taking the time-average of the plots in the top two panels. Time-average is taken from $\Omega t = 100$–300, except for the $\beta_0 = 10^5$ case, which is taken from $\Omega t = 250$–450.

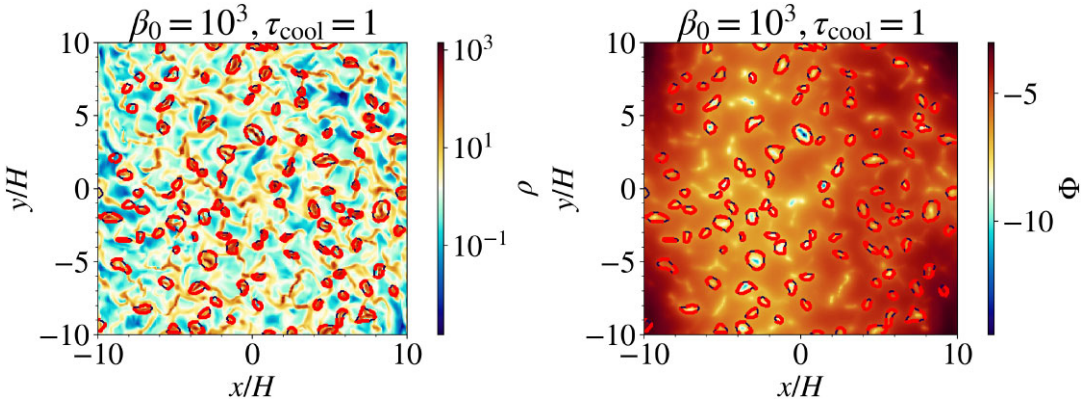

Figure 17. Snapshots of the mid-plane ρ (left) and Φ (right) taken at $\Omega t = 200$ with contours overlaid to indicate clumps identified, taken from simulation with $\beta_0 = 10^3$, $\tau_{\rm cool} = 1$ and low shearing parameter $q = 0.1$.

5.5 Fragmentation in low shear environment

It was mentioned in Kubli et al. (2023) that a number of clumps were formed in the low shear q locations of their simulation. Radial fields in low shear environments take much longer to be sheared into the toroidal direction, potentially alleviating the issue proposed by Gammie (1996) (and discussed in Section 4.1). We repeated one of our simulations ($\beta_0 = 10^3$, $\tau_{\rm cool} = 1$) with very weak shear $q = 0.1$, finding drastically enhanced fragmentation (Fig. 17) and a much larger bound mass fraction of 0.428. However, MRI is very inefficient in low shear environments, and the in-disc field generated in our simulation is weak. Thus, it is unlikely that the magnetic field would have an effect on gravitational instability in our low q simulation; the increased fragmentation seen in this simulation is likely due to stronger growth rates with weaker Coriolis stabilization (Kim & Ostriker 2001).

6 DISCUSSION AND CONCLUSIONS

In this study, we performed local shearing box simulations incorporating a net vertical flux and cooling using a $\tau_{\rm cool}$ prescription (i.e. setting the cooling time to be some constant multiple of Ω^{-1}) (Gammie 2001). By fixing the cooling time to a small value ensuring fragmentation in the weakly magnetized cases, we systematically vary the initial mid-plane plasma beta β_0, which introduces different magnetic field strengths and structures in the saturated stage. We seek to address whether magnetic field promotes or suppresses fragmentation in AGN disc environments. Theoretically, while magnetic pressure tends to suppress GI (as manifested in magneto-Jeans type modes), magnetic tension in a shearing disc context can enhance GI. We call this the Coriolis-Restricted-Magneto-Gravitational (CRMG) instability, and performed WKB stability analysis of the axisymmetric CRMG modes. In this analysis, we find that the instability occurs even for Q_T, $Q_{T,B} > 1$ (compared to magneto-Jeans instability which is unstable only for $Q_{T,B} < 1$), but requires a moderate radial contribution (b_x) to the in-disc magnetic field in order for the magnetic field to have a substantial destabilizing influence (see Fig. 4 and discussion in Section 4.1). This may not be achievable in set-ups with weak vertical flux but is possible with strong vertical flux. We observe in strong vertical flux simulations that the large-scale radial field can achieve $\beta_x \sim 3$, $b_x \sim 0.35$, and the MRI-dynamo seems to be successful in producing a relatively time-steady radial field supporting the use of the WKB analysis. These seem to be promising ingredients for magnetic fields to be destabilizing. However, our simulation results suggest otherwise:

(i) The bound mass fraction drops drastically in the low β_0 cases, where the in-disc magnetic field, produced by the MRI-dynamo, is strong.

(ii) Despite MRI being able to produce sustained in-disc magnetic field with appreciable radial contribution, magnetic elevation due to strong fields produced by the MRI-dynamo causes the mid-plane to be evacuated, increasing the Toomre parameter and lowering the growth rates of potential CRMG modes. This washes out potential increase in growth rates due to increased magnetic field.

Therefore, our conclusion is that magnetic field seems to suppress rather than promote fragmentation in AGN disc environments.

The conclusions drawn in this study rely very much on the horizontally (x, y) averaged quantities. However, local variations across the disc could introduce subtle effects. For example, spiral density waves tend to align the local magnetic field in the direction of the wavefront (Riols & Latter 2019), increasing or decreasing the local radial field contribution b_x depending on the orientation of the waves. Since these waves could harbour density seeds for gravitational instability, this alignment could promote or suppress fragmentation through axisymmetric CRMG growth. However, spiral density waves typically require a moderately low Toomre $Q_T \lesssim 1 - 2$ to accentuate the amplitude (Goldreich & Lynden-Bell 1965), thus it is hardly a relevant issue in our low β_0 simulations, for which $Q_T \gtrsim 3$ as a result of magnetic elevation. Indeed, we hardly observe any spiral waves in our low β_0 test cases.

A recent study by Kubli et al. (2023), using global simulations of a protoplanetary disc, reached different conclusions than ours, that magnetic field is conducive rather than oppressive to clump formation. In particular, they discovered clumps of smaller mass and size in their simulations with magnetic field compared to the case without, indicative of the CRMG instability. This seemingly contradictory result to ours can be resolved by noting that (1) most of their clumps are formed at regions of low shear (i.e. small q), where non-axisymmetric wavevectors and radially pointing magnetic field can maintain their directionality much longer, conducive to the development of the CRMG instability. (2) The magnetic field is primarily generated through the GI-dynamo, not MRI. (3) There is strong resistivity in their simulations. (4) The magnetic field is sub-thermal at the locations of the clumps, implying absence of magnetic elevation. There are no explicit resistivity effects in our simulations

and magnetic field is primarily generated through MRI, not GI, as indicated by the hugely subdominant gravitational stress. In our simulation with a smaller shear parameter $q = 0.1$, we find that the lower shear renders a slower MRI-dynamo and weaker in-disc fields, thus the effect of magnetic field is not as apparent. The presence of resistivity and the use of a global geometry could also change this picture, as one can imagine strong magnetic field being generated in high shear regions, which diffuses to the low shear regions, providing sufficient field strength to trigger the CRMG instability. Our local, ideal MHD set-up cannot address these issues, which we relegate to future work.

ACKNOWLEDGEMENTS

We acknowledge support from NASA Astrophysics Theory Programme grants 80NSSC22K0828 and 80NSSC24K0940, and NASA FINESST Fellowship 80NSSC22K1753 (HGD). The simulations presented in this study were performed using Frontera at TACC under the LRAC computing allocation AST-21007. We also thank the anonymous reviewer for the suggestions, which helped improve this manuscript.

DATA AVAILABILITY

The data used for this study is available upon reasonable request to the authors.

REFERENCES

Bai X.-N., Stone J. M., 2013, ApJ, 767, 30
Balbus S. A., Hawley J. F., 1998, Rev. Mod. Phys., 70, 1
Begelman M. C., Silk J., 2017, MNRAS, 464, 2311
Béthune W., Latter H., 2022, A&A, 663, A138
Chen Y.-X., Jiang Y.-F., Goodman J., Ostriker E. C., 2023, ApJ, 948, 120
Davis S. W., Stone J. M., Pessah M. E., 2010, ApJ, 713, 52
Deng H., Mayer L., Latter H., 2020, ApJ, 891, 154
Deng H., Mayer L., Helled R., 2021, Nat. Astron., 5, 440
Elmegreen B. G., 1987, ApJ, 312, 626
Fromang S., 2005, A&A, 441, 1
Fromang S., Balbus S. A., Terquem C., De Villiers J.-P., 2004, ApJ, 616, 364
Gammie C. F., 1996, ApJ, 462, 725
Gammie C. F., 2001, ApJ, 553, 174
Goldreich P., Lynden-Bell D., 1965, MNRAS, 130, 125
Gong H., Ostriker E. C., 2011, ApJ, 729, 120
Goodman J., 2003, MNRAS, 339, 937
Guo M., Quataert E., Squire J., Hopkins P. F., Stone J. M., 2025, preprint (arXiv:2505.12671)
Hawley J. F., Guan X., Krolik J. H., 2011, ApJ, 738, 84
Hopkins P. F., 2015, MNRAS, 450, 53
Hopkins P. F. et al., 2024, Open J. Astrophys., 7, 20
Jiang Y.-F., Goodman J., 2011, ApJ, 730, 45
Julian W. H., Toomre A., 1966, ApJ, 146, 810
Kim W.-T., Ostriker E. C., 2001, ApJ, 559, 70
Kim J., Ryu D., 2001, ApJ, 561, L135
Kim W.-T., Ostriker E. C., Stone J. M., 2003, ApJ, 599, 1157
Kim C.-G., Kim W.-T., Ostriker E. C., 2011, ApJ, 743, 25
Koyama H., Ostriker E. C., 2009, ApJ, 693, 1316
Kratter K., Lodato G., 2016, ARA&A, 54, 271
Kratter K. M., Matzner C. D., Krumholz M. R., Klein R. I., 2010, ApJ, 708, 1585
Kubli N., Mayer L., Deng H., 2023, MNRAS, 525, 2731
Levin Y., 2007, MNRAS, 374, 515
Löhnert L., Peeters A. G., 2023, A&A, 677, A173
Lynden-Bell D., 1966, The Observatory, 86, 57
Mao S. A., Ostriker E. C., Kim C.-G., 2020, ApJ, 898, 52
McKernan B. et al., 2018, ApJ, 866, 66
Menou K., Quataert E., 2001, ApJ, 552, 204
Meru F., Bate M. R., 2010, MNRAS, 406, 2279
Newcomb W. A., 1961, Phys. Fluids, 4, 391
Parker E. N., 1966, ApJ, 145, 811
Rice W. K. M., Lodato G., Armitage P. J., 2005, MNRAS, 364, L56
Riols A., Latter H., 2018, MNRAS, 474, 2212
Riols A., Latter H., 2019, MNRAS, 482, 3989
Riols A., Lesur G., 2019, A&A, 625, A108
Riols A., Xu W., Lesur G., Kunz M. W., Latter H., 2021, MNRAS, 506, 1407
Salvesen G., Simon J. B., Armitage P. J., Begelman M. C., 2016, MNRAS, 457, 857
Shlosman I., Begelman M. C., Frank J., 1990, Nature, 345, 679
Squire J., Quataert E., Hopkins P. F., 2025, Open J. Astrophys., 8, 39
Stone J. M., Tomida K., White C. J., Felker K. G., 2020, ApJS, 249, 4
Tchekhovskoy A., Narayan R., McKinney J. C., 2011, MNRAS, 418, L79
Toomre A., 1964, ApJ, 139, 1217
Xu W., Jiang Y.-F., Kunz M. W., Stone J. M., 2025, ApJ, 986, 17

APPENDIX A: INITIAL EQUILIBRIUM PROFILE

Under the assumption of a uniform magnetic field, no x, z flow and that ρ, P_g depend only on z, the x-component of equation (2) gives the equilibrium velocity profile $\mathbf{v} = -q\Omega x\hat{\mathbf{y}}$ and the z-component gives the following equation:

$$\frac{1}{\rho}\frac{\mathrm{d}P_g}{\mathrm{d}z} = -\Omega^2 z - 4\pi G\int_0^z \rho\,\mathrm{d}z'. \tag{A1}$$

equation (A1) can be solved using the method described in Jiang & Goodman (2011) and Chen et al. (2023). Assuming a polytropic EOS of $P_g \propto \rho^{5/3}$, we can simplify equation (A1) by transforming into Lane–Emden variables $\rho = \rho_0\theta^{3/2}$, $P_g = P_{g0}\theta^{5/2}$, $\xi = z/h$, where ρ_0, P_{g0} are the initial mid-plane density and gas pressure, giving

$$\frac{\mathrm{d}^2\theta}{\mathrm{d}\xi^2} + \theta^{3/2} = -\frac{Q}{2}. \tag{A2}$$

In doing so, we have defined $h^2 = 5P_{g0}/8\pi G\rho_0^2$, $Q = \Omega^2/2\pi G\rho_0$. Equation (A2) can be solved numerically with the conditions $\theta(0) = 1, \theta'(0) = 0$. In Fig. A1, we see that self-gravity confines the disc profile. Equation (A2) shows that the density and gas pressure profiles, which are encoded in θ, depend only on Q.

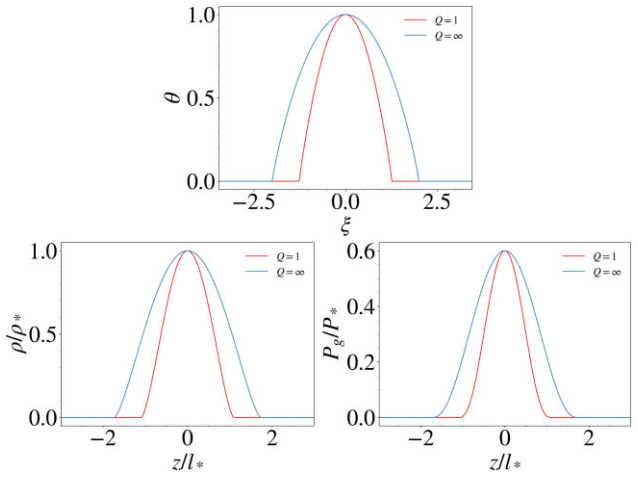

Figure A1. Normalized profiles of θ (top), ρ/ρ_* (bottom left) and P_g/P_* (bottom right) for $Q = 1$. Profiles for the non-self-gravitating case, $Q = \infty$, are shown for comparison.

To calculate ρ, P_g, we need to know ρ_0, P_{g0}. The initial profile is completely specified when the proxy Toomre parameter Q, the surface density Σ and the angular velocity Ω are specified. Once the θ profile is determined from equation (A2), ρ_0, P_{g0} can be calculated using the fact that $\Sigma = 2\rho_0 h \int_0^\infty \theta^{3/2}\,\mathrm{d}\xi$ and $Q = \Omega^2/2\pi G\rho_0$, which gives

$$\rho_0 = \frac{\Omega^2}{2\pi G Q}, \quad P_{g0} = \frac{2\Sigma\Omega^2}{5\Psi_{3/2}Q}, \quad T_0 = \left(\frac{\mu m_p}{k_B}\right)\frac{4\pi G\Sigma}{5\Psi_{3/2}}, \tag{A3}$$

where $\Psi_{3/2}(Q) = \int_0^\infty \theta^{3/2}\,\mathrm{d}\xi$ is a dimensionless measure of the disc's thickness. For $Q \ll 1$, self-gravity dominates and $\Psi_{3/2}$ will be small, while for $Q \gg 1$ the tidal potential dominates, equation (A2) becomes independent of Q and $\Psi_{3/2}$ approaches a constant.

One can observe that Q and the Toomre parameter $Q_T = \langle c_s^2\rangle_\rho^{1/2}\Omega/\pi G\Sigma$ are related in the initial profile. Note that

$$\langle c_s^2\rangle_\rho = \frac{\gamma\int P_g\,\mathrm{d}V}{\int\rho\,\mathrm{d}V} = \frac{c_{s0}^2\int_0^\infty\theta^{5/2}\,\mathrm{d}\xi}{\int_0^\infty\theta^{3/2}\,\mathrm{d}\xi} = c_{s0}^2\frac{\Psi_{5/2}(Q)}{\Psi_{3/2}(Q)}, \tag{A4}$$

$$\Sigma = \int\rho\,\mathrm{d}z = 2\rho_0 h\int_0^\infty\theta^{3/2}\,\mathrm{d}\xi = 2\rho_0 h\Psi_{3/2}(Q), \tag{A5}$$

where $c_{s0} = \sqrt{\gamma P_{g0}/\rho_0}$ is the initial mid-plane sound-speed and $\Psi_{5/2}(Q) = \int_0^\infty\theta^{5/2}\,\mathrm{d}\xi$ is another measure of the disc thickness. Then, we have:

$$Q_T = \frac{c_{s0}\Omega}{2\pi G\rho_0 h}\frac{\left(\Psi_{5/2}\right)^{1/2}}{\left(\Psi_{3/2}\right)^{3/2}} = \left(\frac{8\gamma}{5}Q\right)^{1/2}\frac{\left(\Psi_{5/2}\right)^{1/2}}{\left(\Psi_{3/2}\right)^{3/2}}. \tag{A6}$$

We note that $\Psi_{5/2}$, $\Psi_{3/2}$ depend only on Q and $(\Psi_{5/2})^{1/2}/(\Psi_{3/2})^{3/2}$ is of order unity generally, so Q_T is a function of Q alone and scales roughly as $Q^{1/2}$. For $Q = 1$, $Q_T = 0.89$. In addition, with our choice of units, the initial density and pressure profiles in code units are completely specified by Q.

APPENDIX B: RATIONALE FOR OUR CHOICE OF BOX SIZE

Our choice of box size is unprecedentedly large in local shearing box simulations. Nevertheless, it is numerically justified. First of all, gravitational instability is a long-range effect, so a horizontally extended box is warranted. A common measure of the length-scale required for gravitational effects to be important is the Toomre-length $L_T = \pi^2 G\Sigma/\Omega^2$ (Chen et al. 2023), corresponding to the 2D Jeans length $c_s^2/G\Sigma$. In our initial setup the ratio L_T/H is given by

$$\frac{L_T}{H} = \frac{\pi}{Q_T}\left(\frac{\Psi_{5/2}}{\Psi_{3/2}}\right)^{1/2}, \tag{B1}$$

where $\Psi_{5/2}$ and $\Psi_{3/2}$ are defined in Appendix A and H is the initial mid-plane scale height c_{s0}/Ω. For $Q_T = 0.89$, $L_T/H = 3.2$, which sets a box size of $20H$ roughly to $6.25L_T$. The horizontally averaged Toomre length is unchanged throughout the simulation as $\langle\Sigma\rangle_{xy} = \int\rho\,\mathrm{d}V\,/L_xL_y$ is constant since the total mass is fixed. Thus, our horizontal box size should be sufficient to encompass gravitational effects throughout the simulations. We note that it is typical to use a horizontal box length of $20H$ in existing studies (e.g. Riols & Latter 2019; Löhnert & Peeters 2023).

A large vertical box height is necessary to encompass a sufficient number of scale heights, especially in the strongly magnetized regime where magnetic elevation is active. In the most strongly magnetized case, $\beta_0 = 10$, we find that the mid-plane scale height c_{s0}/Ω is elevated by roughly 4 times compared to the initial value, so an initial vertical extent of $24H$ covers roughly 6 scale heights in the nonlinear stage for that case. We find that simulations that are not sufficiently extended vertically tend to have unphysically dominant Reynolds stresses α_R.

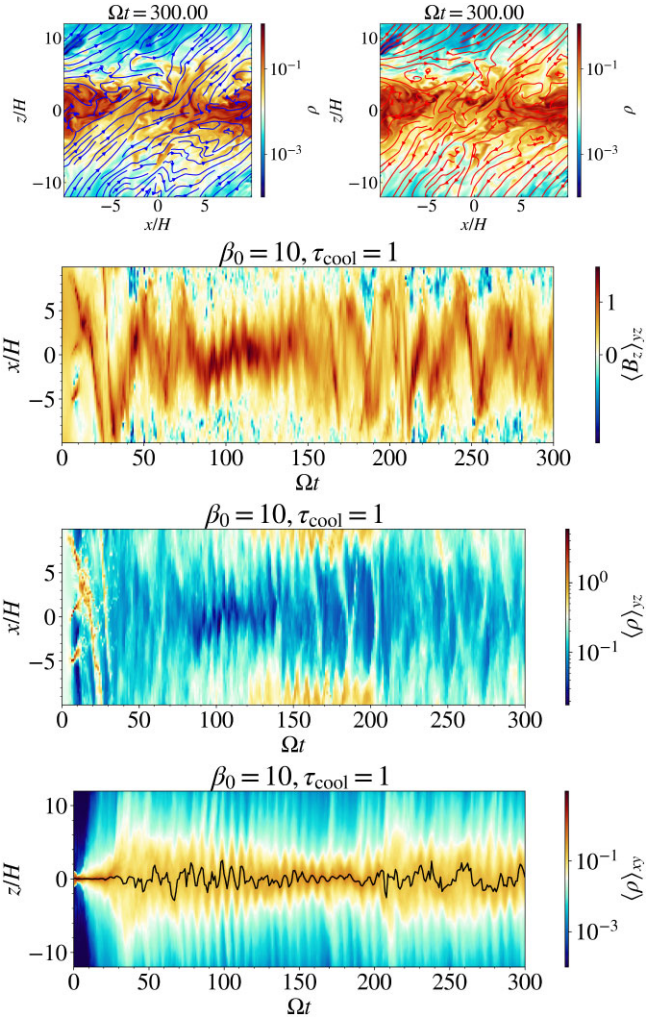

Figure B1. Strong magnetic flux channels develop when a restrictive box ($20H \times 20H \times 24H$) is used. Top row: x–z density slice of the $\beta_0 = 10$, $\tau_{\rm cool} = 1$ case at $\Omega t = 300$, overplotted with magnetic field (top left, blue) and velocity field streamlines (top right, red). Remaining panels: Time-series diagrams of $\langle B_z\rangle_{yz}$ (second row), $\langle\rho\rangle_{yz}$ (third row), $\langle\rho\rangle_{xy}$ (bottom). The black solid line in the bottom panel denotes the density maximum, which oscillates in position. In the second and third row, y–z average $\langle\cdot\rangle_{yz}$ is taken across the whole azimuthal ($-10H < y < 10H$) extent, and only through the disc portion in the vertical ($-2H < z < 2H$) extent. The $x - y$ average $\langle\cdot\rangle_{xy}$ is taken across the full horizontal ($-10H < x, y < 10H$) extent. Note that the direction of variation in the second and third rows are in the x-direction whereas it is in the z-direction for the bottom row.

When running our low $\beta_0 = 10$, 10^2 simulations using a reduced box domain of $20H \times 20H \times 24H$ (resolution of $256 \times 256 \times 512$), we observed signatures of zonal flow described in Riols & Lesur (2019), in which a flux channel stretching diagonally across the $x - z$ plane is formed (Fig. B1). This channel is magnetically enhanced and lower in density than the mid-plane disc material on the two sides, as shown by the slice plots at the top of the figure and the time-series plots of B_z, ρ, averaged over the $y - z$ directions. Over the course of the simulation, we observe disc material on the two

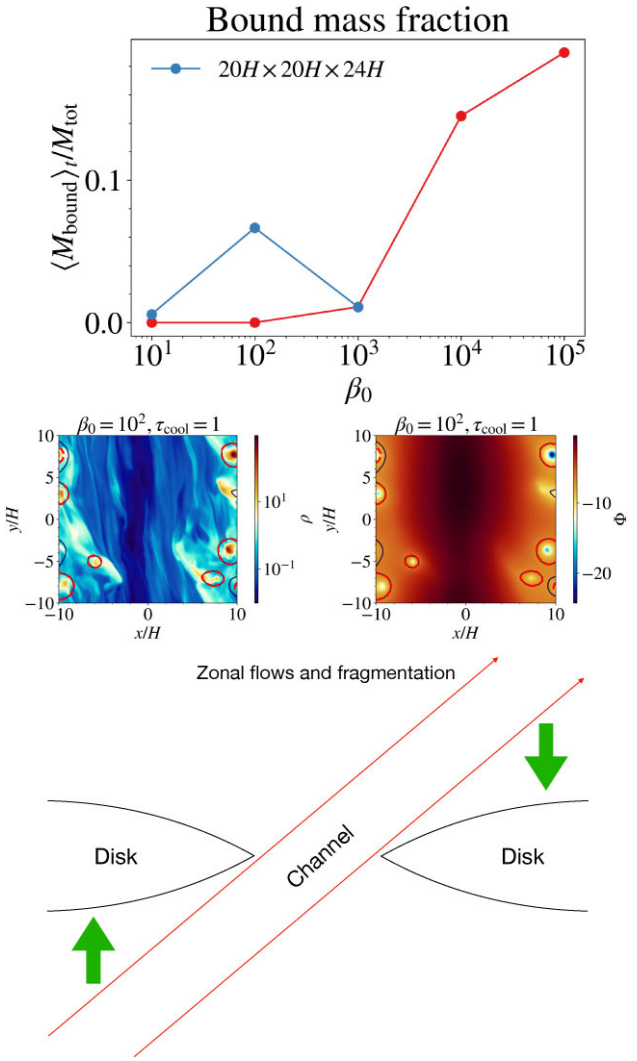

Figure B2. Top: Bound mass fraction for various β_0 using the fiducial box domain and resolution (red), compared against when a more restrictive box $20H \times 20H \times 24H$ (resolution $256 \times 256 \times 512$) is used (blue). Middle two panels: Snapshots of the density and gravitational potential for the case $\beta_0 = 100$, $\tau_{\rm cool} = 1$ when the more restrictive box is used. Bottom: Schematic diagram showing how the ram and magnetic pressure from the channels inhibits gas escape, reinforcing a denser disc, thereby promoting fragmentation.

sides attempting to replenish the channel through turbulent diffusion, occasionally closing it. But it would soon be reopened again by the magnetically driven wind. When a channel is formed, the disc also undulates, as shown by the time-series plot of the $x - y$ averaged density in the bottom panel, where the undulations are marked by the black solid line. Riols & Lesur (2019) explained the origin of such zonal flows as being due to the magnetically driven wind drawing out mass faster than it can be replenished by turbulent diffusion, leading to an instability. The eigenmode of this instability is a diagonal channel, just like the ones we see. Overall, our observations of the zonal structures agree with this explanation. Curiously, when we extend the box domain azimuthally to $20H \times 40H \times 24H$ (resolution of $256 \times 512 \times 384$), the zonal structure is subdued. This could be due to the extra azimuthal freedom giving the turbulence more room to act, closing the channel whenever it begins to form.

Apparently, the channels seen in the zonal flow have an effect on fragmentation. In Fig. B2, we see from the bound mass fraction plot that simulations with a reduced azimuthal extent (where zonal flow is seen), have slightly different fragmentation characteristics (blue line) from the simulations with the fiducial box domain (red line). In particular, the bound mass fraction of the $\beta_0 = 10^2$ case is greatly enhanced. Looking at a snapshot of this simulation, we observe that most of the fragmentation occurs on the sides, away from the channel. We believe that this enhancement in fragmentation is due to the flux channel forming a ram pressure and magnetic pressure wall preventing escape of material, forcing it back to the disc, and increasing the mid-plane density, which is conducive to more fragmentation (see bottom panel of Fig. B2). While this is an interesting observation from a fragmentation point of view, the properties of these flux channels, e.g. their width, how regularly they appear, etc. in a global, astrophysical context are poorly understood. Thus in this study we choose a box domain in which the zonal flow is subdued, and relegate study of the effect of zonal flows on fragmentation to the future.

APPENDIX C: LINEAR ANALYSIS OF THE CORIOLIS-RESTRICTED-MAGNETO-GRAVITATIONAL INSTABILITY FOR A RAZOR-THIN DISC

In this appendix, we outline the linear stability analysis of a self-gravitating, razor-thin disc subjected to an in-plane magnetic field. We refer the reader to Elmegreen (1987), Gammie (1996), and Kim & Ostriker (2001) for more details of this derivation. The fluid equations governing the dynamics of a razor thin disc $\rho = \Sigma\delta(z)$, written out in component form in shearing box coordinates, are

$$\frac{\partial \Sigma}{\partial t} + \left(v_x \frac{\partial}{\partial x} + v_y \frac{\partial}{\partial y}\right)\Sigma + \Sigma\left(\frac{\partial v_x}{\partial x} + \frac{\partial v_y}{\partial y}\right) = 0, \tag{C1}$$

$$\frac{\partial B_x}{\partial t} = B_y \frac{\partial v_x}{\partial y} - v_x \frac{\partial B_x}{\partial x} - v_y \frac{\partial B_x}{\partial y} - B_x \frac{\partial v_y}{\partial y}, \tag{C2}$$

$$\frac{\partial B_y}{\partial t} = B_x \frac{\partial v_y}{\partial x} - v_x \frac{\partial B_y}{\partial x} - v_y \frac{\partial B_y}{\partial y} - B_y \frac{\partial v_x}{\partial x}, \tag{C3}$$

$$\frac{\partial v_x}{\partial t} + \left(v_x \frac{\partial}{\partial x} + v_y \frac{\partial}{\partial y}\right)v_x = -\frac{\partial}{\partial x}(h + \Phi) + \frac{1}{\Sigma}\left(B_x \frac{\partial}{\partial x} + B_y \frac{\partial}{\partial y}\right)B_x - \frac{1}{\Sigma}\frac{\partial}{\partial x}\left(\frac{B^2}{2}\right) + 2\Omega v_y, \tag{C4}$$

$$\frac{\partial v_y}{\partial t} + \left(v_x \frac{\partial}{\partial x} + v_y \frac{\partial}{\partial y}\right)v_y = -\frac{\partial}{\partial y}(h + \Phi) + \frac{1}{\Sigma}\left(B_x \frac{\partial}{\partial x} + B_y \frac{\partial}{\partial y}\right)B_y - \frac{1}{\Sigma}\frac{\partial}{\partial y}\left(\frac{B^2}{2}\right) - 2\Omega v_x, \tag{C5}$$

where $P_g = K\Sigma^\gamma$ is the gas pressure at the disc (K being a constant) and $h = \gamma/(\gamma - 1)K\Sigma^{\gamma-1}$ is the enthalpy density. Defining the disc sound speed by $c_s^2 = \gamma P_g/\Sigma$, it follows that $\partial_i h = \partial_i P_g/\Sigma$ for $i = x, y$. Equations (C1)–(C5) can be derived by integrating the hydrodynamic equations (1)–(4) through z assuming a razor thin density distribution $\rho = \Sigma\delta(z)$ and then expanding in component form. Σ is the surface density of the disc. These equations are coupled to the Poisson equation

$$\nabla^2 \Phi_{\rm 3D}(r, \phi, z) = 4\pi G \Sigma \delta(z), \tag{C6}$$

where $\nabla^2 = \partial^2/\partial x^2 + \partial^2/\partial y^2 + \partial^2/\partial z^2$ here. The gravitational potential in equation (C6), $\Phi_{\rm 3D}$, is related to that in equation (C4), (C5) by $\Phi = \Phi_{\rm 3D}(x, y, z = 0)$. Consider an unperturbed solution (denoted by subscript 0) where $\Sigma_0 = $ const., $\mathbf{v}_0 = -q\Omega x\hat{\mathbf{y}}$,

$P_{g0} = \text{const.}$ with a spatially uniform magnetic field $\mathbf{B}_0 = B_{x0}\hat{\mathbf{x}} + B_{y0}\hat{\mathbf{y}}$. We perturb the fluid variables $Q = Q_0 + Q_1$, where $Q = \Sigma, B_x, B_y, v_x, v_y, h, \Phi$. Keeping only the terms first order in the perturbation, equations (C1)–(C5) become

$$\frac{\partial \Sigma_1}{\partial t} - q\Omega x\frac{\partial \Sigma_1}{\partial y} + \Sigma_0\left(\frac{\partial v_{x1}}{\partial x} + \frac{\partial v_{y1}}{\partial y}\right) = 0, \tag{C7}$$

$$\frac{\partial B_{x1}}{\partial t} = B_{y0}\frac{\partial v_{x1}}{\partial y} + q\Omega x\frac{\partial B_{x1}}{\partial y} - B_{x0}\frac{\partial v_{y1}}{\partial y}, \tag{C8}$$

$$\frac{\partial B_{y1}}{\partial t} = -q\Omega B_{x1} + B_{x0}\frac{\partial v_{y1}}{\partial x} + q\Omega x\frac{\partial B_{y1}}{\partial y} - B_{y0}\frac{\partial v_{x1}}{\partial x}, \tag{C9}$$

$$\begin{aligned}\frac{\partial v_{x1}}{\partial t} - q\Omega x\frac{\partial v_{x1}}{\partial y} &= -\frac{\partial}{\partial x}(h_1 + \Phi_1) + 2\Omega v_{y1}\\ &+ \frac{1}{\Sigma_0}\left(B_{x0}\frac{\partial B_{x1}}{\partial x} + B_{y0}\frac{\partial B_{x1}}{\partial y}\right)\\ &- \frac{1}{\Sigma_0}\frac{\partial}{\partial x}\left(B_{x0}B_{x1} + B_{y0}B_{y1}\right),\end{aligned} \tag{C10}$$

$$\begin{aligned}\frac{\partial v_{y1}}{\partial t} - q\Omega v_{x1} - q\Omega x\frac{\partial v_{y1}}{\partial y} &= -\frac{\partial}{\partial y}(h_1 + \Phi_1) - 2\Omega v_{x1}\\ &+ \frac{1}{\Sigma_0}\left(B_{x0}\frac{\partial B_{y1}}{\partial x} + B_{y0}\frac{\partial B_{y1}}{\partial y}\right)\\ &- \frac{1}{\Sigma_0}\frac{\partial}{\partial y}\left(B_{x0}B_{x1} + B_{y0}B_{y1}\right).\end{aligned} \tag{C11}$$

The perturbed Poisson equation is

$$\nabla^2\Phi_{3D,1} = 4\pi G\Sigma_1\delta(z). \tag{C12}$$

C1 Axisymmetric perturbations

We first consider axisymmetric perturbations ($k_y = 0$). Assuming perturbations have the form $Q_1 \propto \exp(ik_x x - i\omega t)$, equations (C7)–C11 become

$$\omega\Sigma_1 = k_x\Sigma_0 v_{x1}, \tag{C13}$$

$$B_{x1} = 0, \tag{C14}$$

$$\omega B_{y1} = k_x B_{y0}v_{x1} - k_x B_{x0}v_{y1}, \tag{C15}$$

$$\left(\omega - k_x^2 v_{Ay}^2/\omega\right)v_{x1} = k_x(h_1 + \Phi_1) - \frac{k_x^2 v_{Ax}v_{Ay}}{\omega}v_{y1} + 2i\Omega v_{y1} \tag{C16}$$

$$\omega v_{y1} = -\frac{k_x^2 v_{Ax}v_{Ay}}{\omega}v_{x1} + \frac{k_x^2 v_{Ax}^2}{\omega}v_{y1} + i(q-2)\Omega v_{x1}, \tag{C17}$$

where $c_s^2 = \gamma P_g/\Sigma_0$, $v_A^2 = B_0^2/\Sigma_0$ are the sound speed and Alfvén speed, respectively. The perturbed Poisson equation becomes

$$\frac{\partial^2\Phi_{3D,1}}{\partial z^2} = k_x^2\Phi_{3D,1} + 4\pi G\Sigma_1\delta(z). \tag{C18}$$

The solution to the perturbed Poisson equation (C18) is

$$\Phi_{3D,1} = -\frac{2\pi G\Sigma_1}{|k|}e^{-|kz|}, \tag{C19}$$

which gives $\Phi_1 = \Phi_{3D,1}(x, y, z = 0) = -2\pi G\Sigma_1/|k|$. The perturbed enthalpy density is $h_1 = c_s^2\Sigma_1/\Sigma_0$. Substituting into equations (C13)–C17 and rearranging gives the following dispersion relation

$$\begin{aligned}&\omega^4 + \left[2(q-2)\Omega^2 - k_x^2\left(c_s^2 + v_A^2\right) + 2\pi G\Sigma_0|k_x|\right]\omega^2\\ &+ iq\Omega\omega k_x^2 v_{Ax}v_{Ay}\\ &+ k_x^2 v_{Ax}^2\left(k_x^2 c_s^2 - 2\pi G\Sigma_0|k_x|\right) = 0. \quad \text{(Razor-thin disk)}\end{aligned} \tag{C20}$$

If the background density is uniform with value ρ_0 instead of razor-thin, one simply needs to replace the $2\pi G\Sigma_0|k_x|$ terms in equation (C20) by $4\pi G\rho_0$, i.e.

$$\begin{aligned}&\omega^4 + \left[2(q-2)\Omega^2 - k_x^2\left(c_s^2 + v_A^2\right) + 4\pi G\rho_0\right]\omega^2\\ &+ iq\Omega\omega k_x^2 v_{Ax}v_{Ay}\\ &+ k_x^2 v_{Ax}^2\left(k_x^2 c_s^2 - 4\pi G\rho_0\right) = 0. \quad \text{(Uniform background)}\end{aligned} \tag{C21}$$

APPENDIX D: WAVELENGTH DEPENDENCE OF THE AXISYMMETRIC CRMG INSTABILITY WITH RESPECT TO THE FIELD STRENGTH

In Fig. D1 we show, for two sets of $(Q_T, B_x/B, q)$ parameters, that the wavelength of the most unstable axisymmetric CRMG mode becomes shorter when the magnetic field becomes stronger. The typical most unstable wavelength is roughly a thermal scaleheight (c_s/Ω). The most unstable wavelength is the shortest at $\beta \approx 1$, and increasing the field strength further below $\beta \approx 1$ yields a longer wavelength. Kubli et al. (2023) found that this explains the smaller clumps found in their simulations when magnetic field is introduced.

APPENDIX E: COMPARISON OF THE AXISYMMETRIC CRMG AND MAGNETO-JEANS TYPE MODES

The CRMG mode described above is fundamentally different from the magneto-Jeans type mode in the sense that it is destabilized for stronger magnetic field while the latter is stabilized in that limit. We illustrate this difference in Fig. E1 by comparing the fastest growth rate of the two modes over a range of plasma beta, with the growth rate of the CRMG mode determined by equation (25) and that for the magneto-Jeans type mode determined by $\omega^2 = k_x^2(c_s^2 + v_A^2) + 2(2-q)^2\Omega^2 - 2\pi G|k_x|\Sigma_0$. We performed this exercise for two sets of $(Q_T, B_x/B, q)$ parameters. For each β, the growth rate is calculated over a range of wavenumbers and the maximal one is selected and displayed. At high β, the two modes converge, with both of them stable when $Q_{T,B} > 1$ and unstable otherwise. The growth rate of CRMG mode begins to deviate at $\beta \sim 10^2$, becoming stronger at lower β while Jeans type mode dwindles due to $Q_{T,B} > 1$ at low β.

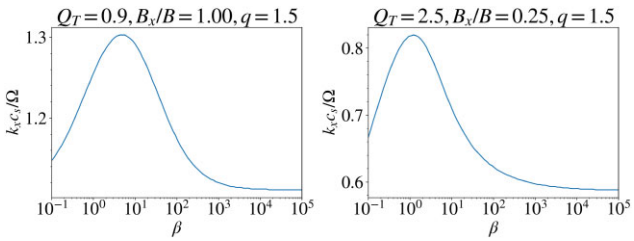

Figure D1. Most unstable axisymmetric wavenumber (expressed as $k_x c_s/\Omega$) for as a function of plasma beta β for two sets of $(Q_T, B_x/B, q)$ parameters.

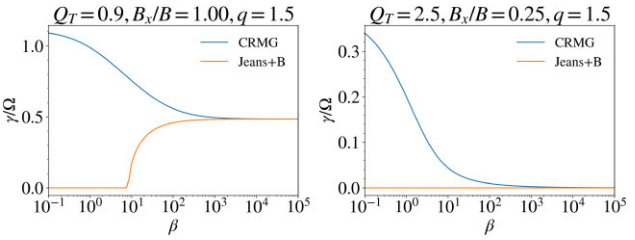

Figure E1. Comparison of growth rates against plasma beta β of the CRMG and magneto-Jeans type unstable modes for two sets of $(Q_T, B_x/B, q)$ parameters. For each β, the the growth rate is calculated over a range of $k_x v_A/\Omega$ and the maximal one is selected and displayed.

In addition, for CRMG modes, the most unstable wavelength varies non-monotonically with respect to the magnetic field strength while it becomes larger with increasing field strength for magneto-Jeans mode[11] In particular, in the regime $\beta > 1$, the most unstable wavelength becomes shorter as β decreases.

APPENDIX F: NUMERICAL VERIFICATION OF THE AXISYMMETRIC CRMG GROWTH RATE IN 2D

We verify that the CRMG instability can be captured by simulation. Using a 2D set-up (without cooling) with background density ρ_0, sound speed c_{s0} and angular frequency Ω set to 1, we inserted an axisymmetric mode with density amplitude of $\delta\rho_{\max}/\rho_0 = 0.01$ into the background and let it evolve. As it is impossible to set up a razor-thin disc in 2D, we redid the linear analysis using a uniform density background. The dispersion relation remains the same as equation (25) except $2\pi G\Sigma_0|k_x|$ is replaced by $4\pi G\rho_0$ (equation C21). The unstable mode we selected for display is characterized by $\Omega^2/4\pi G\rho_0 = 1, k_x v_{A0}/\Omega = 0.5, \beta = 2P_{g0}/P_{B0} = 1, B_{x0}/B_0 = 1, q = 0$. We use a shearing parameter $q = 0$ for this demonstration to keep the background radial field B_x static (a non-zero shearing parameter q would cause B_x to be sheared into the azimuthal direction on a timescale of $(q\Omega)^{-1}$). As we observe in Fig. F1, the perturbed density profile grew exponentially with a growth rate of $\gamma/\Omega = 0.201$, matching the expected growth rate of 0.199. We followed the growth into the nonlinear regime, which is characterized by a single overdense peak.

APPENDIX G: COMPARISON WITH LOWER RESOLUTION SIMULATIONS

We repeated our simulations at a reduced resolution of $128 \times 128 \times 192$ (for $\beta_0 \geq 10^3$) and $128 \times 256 \times 192$ (for $\beta_0 < 10^3$), keeping the box dimensions the same. We present a comparison of the stresses, mid-plane magnetic field, and fragmentation fraction for the two resolutions (HR denoting the fiducial resolution cases, LR denoting the reduced resolution cases). Due to limited computational resources, we could not re-simulate the test cases at a higher resolution. In Table G1 we list the time-averaged quality factors in the y ($\langle Q_y\rangle_t$) and z ($\langle Q_z\rangle_t$) directions at the mid-plane.

[11]Using the dispersion for magneto-Jeans modes: $\omega^2 = k_x^2(c_s^2 + v_A^2) + 2(2-q)^2\Omega^2 - 2\pi G|k_x|\Sigma_0$, the most unstable mode has wavenumber $k_{x,\max} = \pi G\Sigma_0/(c_s^2 + v_A^2)$, which decreases (shifts to longer wavelength) when magnetic pressure dominates. If the background density were uniform instead of razor-thin, the most unstable wavenumber would be $k_{x,\max} = 0$ instead, i.e. the largest scale mode would be the most unstable.

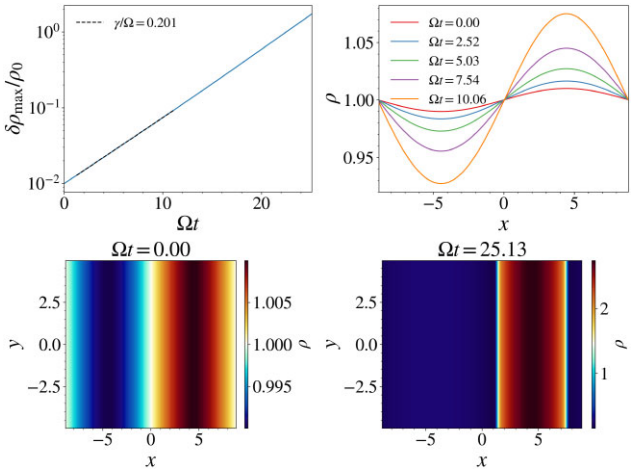

Figure F1. Simulation of a selected CRMG unstable mode with $\Omega^2/4\pi G\rho_0 = 1, k_x v_{A0}/\Omega = 0.5, \beta = 2P_{g0}/P_{B0} = 1, B_{x0}/B_0 = 1, q = 0$, where the subscript 0 denotes the background value. Top left: The growth curve of the mode, measured by $\delta\rho_{\max}/\rho_0 \equiv (\rho_{\max} - \rho_0)/\rho_0$, where $\rho_{\max}$ is the maximum density. The fitted growth rate of $\gamma/\Omega = 0.201$ (black dashed line) is very close to the expected growth rate of 0.199. Top right: snapshots of the density profile in the x-direction during linear growth, showing the perturbed profile growing *in situ*. Bottom left and right: The initial (left) and $\Omega t = 25.13$ (right) 2D density snapshots, showing how the imposed density perturbation grows to non-linear amplitudes.

Table G1. Comparison of the time-averaged quality factors $\langle Q_y\rangle_t, \langle Q_z\rangle_t$ for the fiducial cases (HR) and the reduced resolution cases (LR).

β_0	$\langle Q_y\rangle_t$ (HR)	$\langle Q_y\rangle_t$ (LR)	$\langle Q_z\rangle_t$ (HR)	$\langle Q_z\rangle_t$ (LR)
10	482	189	146	73.3
10^2	391	146	88.2	29.5
10^3	207	122	35.8	11,6
10^4	78.6	68.2	24.8	6.14
10^5	82.5	29.2	28.7	6.10

The quality factors of the lower resolution cases are generally a factor of a few lower than the fiducial cases. For $\beta_0 \geq 10^4$, $\langle Q_z\rangle_t$ are less than 10 for the LR cases, which according to Hawley, Guan & Krolik (2011) means MRI may be under-resolved for those cases.

From Figs G1–G3, we see that the stresses, mid-plane magnetic field, and the bound mass fraction in the LR cases are quite close to the HR cases for $\beta_0 \leq 10^3$. Surprisingly, there are good agreements for the $\beta_0 = 10^5$ case as well except for the Maxwell stress α_M, which is a factor of 2 lower for the LR case, reflecting under-resolved MRI modes.

The behavior of the $\beta_0 = 10^4$ case (LR) is rather odd, as the toroidal plasma beta and Maxwell stress are markedly stronger than in the HR case on average, and the bound mass fraction is exceptionally low. This is contrary to the expectation that under-resolved MRI modes should give rise to weaker Maxwell stress and field amplification, although we note that for $\Omega t \leq 50$ the Maxwell stress of the LR case is smaller. At $\Omega t \sim 50$ the magnetic field increased greatly for the LR case. In Fig. G4, we show the vertical profiles of the toroidal magnetic field (as time-averaged and timeseries plots) of the $\beta_0 = 10^4$ case for the LR and HR resolutions. We note that the toroidal field in the LR, $\beta_0 = 10^4$ case is particularly strong at the mid-plane, and does not exhibit the antisymmetric

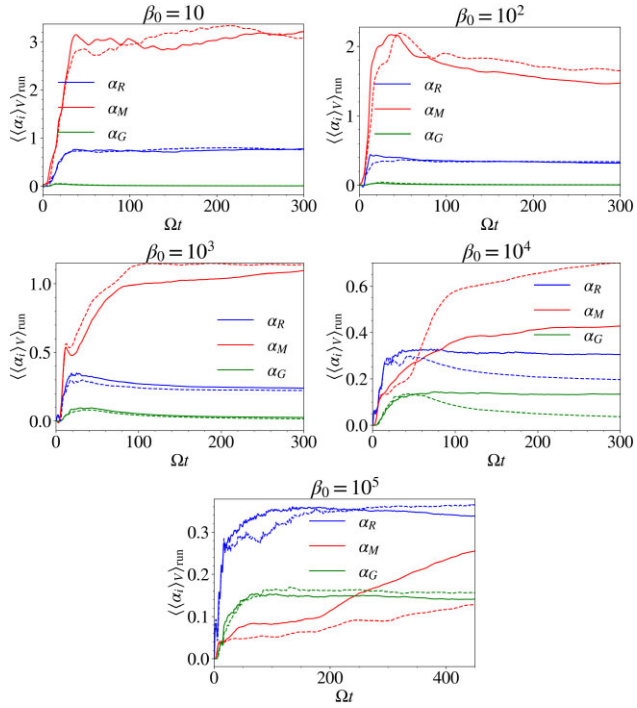

Figure G1. Comparison of the running-averaged stresses for the two resolutions explored. Solid line denotes the fiducial resolution (HR), while dashed lines denotes the reduced resolution (LR). The title in each panel denotes β_0 of the test case.

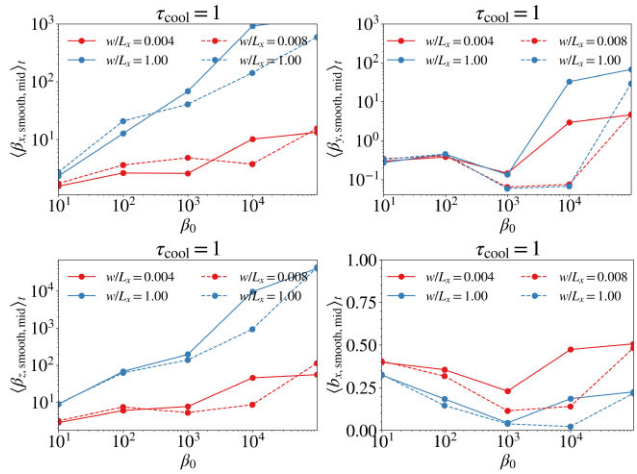

Figure G2. Mid-plane window-averaged, time-averaged radial field plasma beta $\langle \beta_{x,\rm smooth} \rangle_t$ (top left), toroidal plasma beta $\langle \beta_{y,\rm smooth} \rangle_t$ (top right), vertical plasma beta $\langle \beta_{z,\rm smooth} \rangle_t$, and the relative radial field strength $\langle b_{x,\rm smooth} \rangle_t$. Solid line denotes HR resolution, dashed line denotes LR resolution.

profile observed in the HR case. It is unclear to us how lower resolution would trigger the sudden and overwhelming increase in the toroidal field, and why it happens only to the $\beta_0 = 10^4$ case at low resolution. This comparison reinforces our fiducial choice of a higher resolution. We note, that the other β_0 cases appear to be converged with resolution.

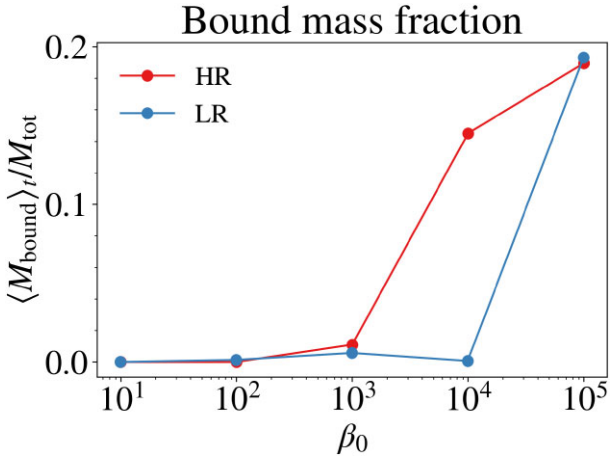

Figure G3. Comarison of the bound mass fraction found in the two resolutions, with the red solid line denoting the fiducial resolution (HR), and the blue solid line denoting the reduced resolution cases (LR).

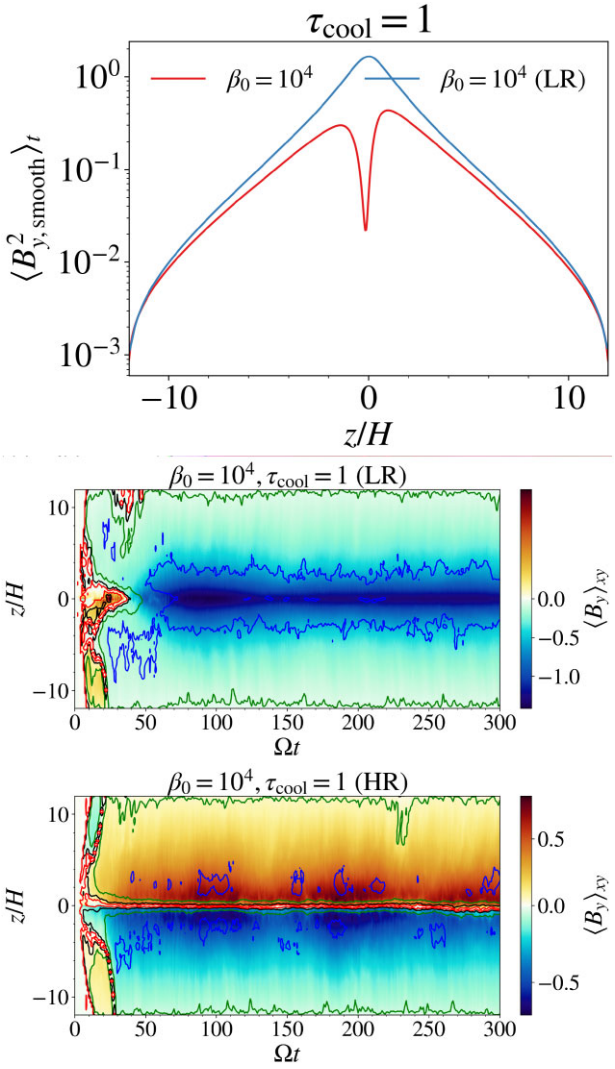

Figure G4. Top: window-averaged, time-averaged B_y^2 profiles for the HR (red) and LR (blue) cases. Bottom: Timeseries diagrams of B_y for the LR, HR cases ($\beta_0 = 10^4$).

This paper has been typeset from a TEX/LATEX file prepared by the author.